

# Swell Generation under Extra-Tropical Storms

M. C. Hell<sup>1</sup>, Alex Ayet<sup>2,3</sup>, Bertrand Chapron<sup>4</sup>

<sup>1</sup>University of California San Diego, Scripps Institution of Oceanography, La Jolla, CA, USA

<sup>2</sup>Climat, Environnement, Couplages, Incertitudes, CECI, Université de Toulouse, CNRS, CERFACS,  
Toulouse, France

<sup>3</sup>CNRM, Université de Toulouse, Météo-France, CNRS, Toulouse, France

<sup>4</sup>Ifremer, CNRS, IRD, Univ. Brest/ Laboratoire d'Océanographie Physique et Spatiale (LOPS), IUEM,  
Brest, France

## Key Points:

- Wave generation by a moving extra-tropical storm is described using a Gaussian wind field and a parametric model of wave development
- A new developed machine-learning algorithm triangulates the space-time evolving source point of swell systems from buoy measurements
- This model describes the distance between swell source and the storm's maximum wind speed and reveals sensitivities to storm's parameters

---

Corresponding author: Momme Hell, [mhell@ucsd.edu](mailto:mhell@ucsd.edu)

**Abstract**

Storms propagate over the ocean and create moving patches of strong winds that generate swell systems. Here, we describe the dynamics of wave generation under a moving storm by using a simple parametric model of wave development, forced by a temporally- and spatially-varying moving wind field. This framework reveals how surface winds under moving storms determine the origin and amplitude of swell events. Swell systems are expected to originate from locations different than the moving high-wind forcing regions. This is confirmed by a physically-informed optimization method that back-triangulates the common source locations of swell using their dispersion slopes, simultaneously measured at five wave-buoy locations. Hence, the parametric moving fetch model forced with reanalysis winds can predict the displacement between the highest winds and the observed swell source area when forced with reanalysis winds. The model further shows that the storm's peak wind speed is the key factor determining swell energy since it determines surface wind gradients that lead to the spatial convergence of wave energy into a much smaller area than the wind fetch. This spatial wave energy convergence implies enhanced wave energy dissipation in this focusing area, slightly displaced from the maximum wind locations. This analysis provides an improved understanding of fetches for extra-tropical swell systems and may help to identify biases in swell forecast models, air-sea fluxes, and upper-ocean mixing estimations.

**Plain Language Summary**

Storms generate waves on the ocean surface that can travel across entire ocean basins, the so-called swell waves. However, it is unclear how the amplitude and period of these surface waves depend on the strength and shape of the storm. One has to consider the movement of the storm in addition to its size, lifetime, and wind speeds. This study shows how all these parameters control the amplitude and period of swell events reaching the coastlines. We find that the storm's movement and its peak wind speed compress the wave energy to a small area, which then appears as a swell source location in the open ocean. This study can help improve swell forecasts and understand how long-term changes in mid-latitude storms would modify the exchange of momentum and heat between the atmosphere and the ocean.

## 46 1 Introduction

47 Swell events are long-crested linear wave systems that propagate across the ocean  
48 basins (Munk & Snodgrass, 1957; Snodgrass et al., 1966; Ardhuin et al., 2009). Swells  
49 impact harbor safety, coastal floating, and beach erosion (Wilson, 1957; Morison & Im-  
50 berger, 1992; Russell, 1993; Hunt, 1961; Ferreira, SPR 2005; Enríquez et al., 2017), but  
51 also modulate sea surface height and affect altimeter and other remote sensing obser-  
52 vations (like future SWOT or ICESat-2, Morrow et al., 2019; Klotz et al., 2020). Import-  
53 tantly, swells play a role in air-sea interactions, possibly altering the sea surface rough-  
54 ness and subsequent turbulent air-sea fluxes (Makin, 2008). In addition, swell systems  
55 trace intense air-sea exchanges, and hence can potentially help to better understand air-  
56 sea fluxes and mixed-layer variability under storms, as well as impacts on global climate.  
57 The motivation of this study is to provide rapid and robust means of swell generation  
58 and how swell events are driven by mid-latitude storm variability.

59 Swell waves are routinely observed, e.g. along coastlines using the Coastal Data  
60 Information Program/National Data Buoy Center (CDIP/NDBC, O’Reilly et al., 2016,  
61 Figure 1b to e), or from space by Synthetic Aperture Radar images (SAR, Chapron et  
62 al., 2001) and Real Aperture Radar measurements (Hauser et al., 2020). These obser-  
63 vations can be used to back-track swell to focal points or swell source locations, either  
64 by utilizing the deep water dispersion relation in spectrograms observed at a point (Munk,  
65 1947; Barber & Ursell, 1948; Snodgrass et al., 1966; Hell et al., 2019) or by estimating  
66 the local convergence of the wave ray’s backward trajectories derived from SAR-images  
67 (Collard et al., 2009; Husson et al., 2012). Both methods assume swell systems to orig-  
68 inate from an idealized source point. Clearly, the definition of such a source point may  
69 appear ambiguous, given typical spatial scales  $O(1000km)$  and lifetime  $O(5 \text{ days})$  of a  
70 extra-tropical storm that moves at about  $10 \text{ m s}^{-1}$  (Figure 1a, Eady, 1949; Hodges et  
71 al., 2011; Neu et al., 2012).

72 A path to understand the appearance of such source points and the properties of  
73 the resulting swell systems, is to analyse the relationship between surface winds and the  
74 resulting surface wave spectra. This relation can generally be well approximated by a  
75 set of semi-empirical functions that assume homogeneous wind speeds within an area or  
76 for a certain duration: the fetch (“fetch laws”, K. Hasselmann et al., 1973, 1976; Elfouhaily  
77 et al., 1997, and there in). However, these self-similar relations, first established by Kitaigorodskii

78 (1962), do not account for the spatial and temporal variability of the wind forcing. It  
 79 is thus unclear how a continuously varying wind field leads to the generation of one dom-  
 80 inant single wave event that seems to stem from a very small source region, at least an  
 81 order of magnitude smaller than the storm (Munk, 1947; Barber & Ursell, 1948; Collard  
 82 et al., 2009; Husson et al., 2012; Hell et al., 2020).

83 Spectral wave models, like Wave Watch III (Tolman, 2009), have also known weak-  
 84 nesses due to their strong dependencies on the wind forcing field (Cavaleri, 1994; Ponce  
 85 & Ocampo-Torres, 1998; Feng et al., 2006; Durrant et al., 2013; Stopa & Cheung, 2014;  
 86 P. A. Janssen & Bidlot, 2018). While parameterizations of the source terms in those nu-  
 87 merical models essentially reproduce the fetch laws, modelled wave arrival times and heights  
 88 are commonly biased compared to in-situ wave-buoy observations. These biases are likely  
 89 related to some lack of precise information to describe storm dynamics. Extreme winds  
 90 may not always be properly described over time and space, and generated swell systems  
 91 cannot always be correctly predicted. This strong dependence of the modelled wave field  
 92 on the wind forcing is also important when wave models are coupled to Earth system  
 93 models to better represent surface fluxes and air-sea exchange (Li et al., 2016; Bourassa  
 94 et al., 2019). In this case, wave model parameters cannot be tuned to compensate for  
 95 biases in the wind forcing, and hence a better dynamical understanding of wave gener-  
 96 ation is still needed to include waves in coupled Earth system models.

97 An alternative to the fetch’s scaling laws or spectral wave models is to consider sim-  
 98 ple wave evolution models, directly compared to wind and wave observations. Numer-  
 99 ous studies have used this strategy for moving tropical cyclones (Young, 1988, 2003; Bowyer  
 100 & MacAfee, 2005; Chen et al., 2007; Young & Vinoth, 2013; Kudryavtsev et al., 2015,  
 101 2021), but the relationship between faster moving extra-tropical storms and resulting  
 102 swell events remains largely unexplored (Figure 1, Young et al., 1987; Doyle, 1995, 2002).  
 103 Extra-tropical storms are an integral part of synoptic meteorology with ample theories  
 104 about their dynamics and life cycles (Bjerknes, 1919; Shapiro & Keyser, 1990; Neiman  
 105 & Shapiro, 1993; Neiman et al., 1993; Schultz et al., 1998; Schemm & Wernli, 2014, re-  
 106 view in ; Schultz et al., (2018)) and here we aim to connect these theories with dynam-  
 107 ics of wave generation.

108 In this study, we explicitly show how synoptic-scale dynamics can be related to prop-  
 109 erties of the generated sea states and the residual swell systems. We build on develop-

110 ments presented in Kudryavtsev et al. (2015) to derive a simplified model for swell events  
 111 from extra-tropical storm (section 2.1). The goal is to complement full sophisticated spec-  
 112 tral wave models, since a simplified model can rapidly provide large ensembles of solu-  
 113 tions to help retrieve the storm properties. More explicitly, we approximate the mov-  
 114 ing fetch with varying winds under an extra-tropical cyclones as a two-dimensional Gaus-  
 115 sian shape and analyse the dynamics resulting from gradients in the wind forcing field  
 116 (section 2.2). We then use a back-triangulating method to retrieve the swell source lo-  
 117 cation from wave buoy observations (sections 3.1 and 3.2). This allows us to test the ide-  
 118 alized moving wind fetch model for several case studies in the North Pacific (sections 3.3  
 119 and 3.4). Combining an idealized model for swell generation and the optimized model  
 120 of swell propagation finally suggests a three stage life-cycle of swell waves that is sum-  
 121 marized and discussed in section 4.

## 122 2 Wave generation in a moving frame of reference

In this section, we extend the framework introduced by Kudryavtsev et al. (2015)  
 to extra-tropical storms. Wave spectra of growing seas are assumed to follow self-similarity,  
 and dynamical changes of the spectra are described by a single variable, the peak an-  
 gular frequency  $\omega_p$  (K. Hasselmann et al., 1976; Kudryavtsev et al., 2015). The evolu-  
 tion of  $\omega_p$  in an Eulerian frame is then described by

$$\frac{\partial \omega_p}{\partial t} + c_g \frac{\partial \omega_p}{\partial x} = \left(\frac{g}{u}\right)^2 \phi(\alpha), \quad (1)$$

where  $c_g = \partial_k \omega_p = g/2 \omega_p$  is the peak group velocity,  $\alpha = u/c_p = u \omega_p/g$  is the wave  
 age, the ratio of the 10-m wind speed  $u$  and phase velocity of the spectral peak  $c_p =$   
 $g/\omega_p$  (Equation A8 in Kudryavtsev et al., 2015). The wind-input source term  $\phi$  is de-  
 fined as

$$\phi(\alpha) = \frac{q}{2} \left(\frac{c_\alpha}{\alpha}\right)^{1/q} \quad (2)$$

123 with  $c_\alpha = 15.4$ , and  $q = -3/10$ . Here, and in the following analysis, we use a set of  
 124 parameters for a so-called young sea development (K. Hasselmann et al., 1976; Badulin  
 125 et al., 2007; Kudryavtsev et al., 2015, details in Appendix A3). In the following, outlined  
 126 dynamics remain the same for all possible choices of these parameters. Note that under  
 127 constant winds Equation (1) is reduced to the familiar “fetch relations” (K. Hasselmann  
 128 et al., 1973, 1976; Elfouhaily et al., 1997, and references therein).

The above equations solely describe the spectral peak variables ( $c_g, c_p$  and  $\omega_p$ ), but this is sufficient to derive the whole wave energy spectrum following semi-empirical relations (K. Hasselmann et al., 1973; Elfouhaily et al., 1997; Pierson & Moskowitz, 1964). The total wave energy  $E$  and significant wave height  $H_s$  of the growing wave field are then related to the peak frequency  $\omega_p$  with

$$\frac{E g^2}{u^4} = \frac{H_s^2 g^2}{16 u^4} = c_e \left( \frac{d g}{u^2} \right)^p \sim \frac{u g^2}{2 \omega_p^3}, \quad (3)$$

129 where  $c_e = 4.41 \times 10^{-7}$  and  $p = 1$ , again following K. Hasselmann et al. (1976), Badulin  
 130 et al. (2007), and Kudryavtsev et al. (2015). For this simple case of stationary wave gen-  
 131 eration, the energy of the generated wave field  $E$  travels with the group velocity  $c_g$  and  
 132 hence can eventually leave the generation area. Over the open ocean, wave generation  
 133 is related to patches of strong winds under storms, called the fetch, that are neither sta-  
 134 tionary nor infinite (Munk, 1947). The standard fetch relations are thus theoretical lim-  
 135 its, and the fetch's characteristic scales and its propagation must be taken into account.

For a storm and its fetch that both moving with the translational speed  $V$ , the wave-  
 growth equation Equation (1) must be written in a Lagrangian frame of reference, mov-  
 ing with the storm as

$$\partial_t \omega_p + (c_g - V) \partial_X \omega_p = \left( \frac{g}{u} \right)^2 \phi(\alpha), \quad (4)$$

136 where  $X = x - Vt$  is the along-wind coordinate in the moving reference frame (Kudryavtsev  
 137 et al., 2015). This equation describes the evolution of a growing sea in the moving frame  
 138 with coordinates  $(X, t)$ , and the forcing  $\phi(u, \omega_p)$  that is a function of the local wind speed  
 139  $u(X, t)$ . This non-linear 1st-order partial differential equation is used in the following  
 140 two subsections to outline the effects of a moving fetch on growing waves for typical scales  
 141 of extra-tropical storms. First for storms with constant winds for which the equation can  
 142 be solved analytically (section 2.1), and then with temporally and spatially varying winds  
 143 following a Gaussian form (section 2.2).

## 144 2.1 Constant, finite moving wind models

145 First, we consider constant steady winds  $u$  under a storm of length  $L$  and dura-  
 146 tion  $T$ , steadily moving with a constant translation velocity  $V$ . Constant winds imply  
 147 a constant forcing function  $\phi(\omega_p)$ , such that Equation 4 can be solved analytically for  
 148  $\omega_p$  using the method of characteristics (Appendix A). Figure 2 shows these character-  
 149 istic curves of wave energy for typical scales of tropical and extra-tropical storms. The

150 characteristic curves  $X(t, X_0, t_0, c_0)$  describe the position of a growing non-linear wave  
 151 packet which has a group speed  $c_0$  at position  $X_0$  and time  $t_0$ , as it passes through the  
 152 forcing field. Their 1st derivatives  $\partial_t X \propto (c_g - V)$  describe wave energy's speed  $c_g$   
 153 relative to the speed of the moving frame  $V$ , and their curvature is proportional to the  
 154 acceleration of this wave field and similarly the intensity of wave energy growth ( $\partial_{tt} X \propto \dot{c}_g \propto \dot{E}$ ).

The initial sea is assumed to be at rest ( $c_0 = 0$ ) such that the wave energy at the beginning of the storm ( $X(t, X_0, 0, 0)$ , Figure 2 bottom axis) is slow and propagates backward in the moving frame of the storm (for example in Figure 2a day 0 to 0.3). Even though these young seas propagate slower than the storm, their energy continues to grow because they are continuously exposed to the steady wind forcing. With time, the peak frequency decreases, and the group velocity of the peak wave energy increases (Equation 3). After a critical time  $\tau_{crit}$  (dashed black line in Figure 2), the peak wave energy starts travelling at the same speed as the storm, i.e.  $c_g = V$ . This timescale from the wind's onset until  $c_g = V$  is

$$\tau_{crit} = \frac{c_\tau}{g} u^{-q} V^{1+\frac{1}{q}}, \quad (5)$$

and the distance the storm has traveled during this time is

$$X_{crit} = \frac{c_\tau}{g} q u^2 \left(\frac{u}{V}\right)^{\frac{1}{q}}, \quad (6)$$

155 where  $c_\tau(c_\alpha, q) = 1.23 \times 10^5$  and  $q = -3/10$  measuring the efficiency of wave growth  
 156 depending on the sea state (Appendix A).

157 While tropical and extra-tropical cyclones may have comparable translation velocities,  
 158 tropical cyclones are smaller in scale, but can create very strong surface wind speeds  
 159 for several days. This leads to a trapping or quasi-resonance of wave energy under tropical  
 160 storms (Kudryavtsev et al., 2015). Trapping also appears under extra-tropical storms  
 161 that are large enough ( $X > X_{crit}$ , Figure 2 red dots), and, more importantly, last long  
 162 enough ( $t > \tau_{crit}$ , Figure 2 dashed black line). Trapping can create more energetic (i.e.  
 163 faster and longer) swell waves, because the growing sea-state remains longer under the  
 164 forcing wind field than it would under a stationary wind field. Hence, only wave energy  
 165 whose characteristic curves originate at a time larger than  $\tau_{crit}$  or at a position larger  
 166 than  $X_{crit}$  can end up propagating to the forefront of the moving fetch and being exposed  
 167 to the maximum possible wind forcing (dark blue lines in Figure 2).

168 The trapping conditions are determined by the wind speed and translation veloc-  
 169 ity (Equation 5 and 6). Figure 2 illustrates how these critical scales differ between fetches  
 170 of tropical cyclones (Figure 2a,  $\tau_{crit} \approx 6$  to 10 hours and  $X_{crit} \approx 50$  to 100 km Kudryavt-  
 171 sev et al., 2015) and extra-tropical cyclones (Figure 2b and c,  $\tau_{crit} \approx 12$  to 36 hours  
 172 and  $X_{crit} \approx 100$  to 400km).

173 The characteristic curves of wave energy under constant moving winds can then  
 174 be separated into curves that leave the storm from the rear ( $X_0 < X_{crit}$ ), curves that  
 175 start further in the front ( $X_0 > X_{crit}$ ) and reach the trapping condition, and finally  
 176 curves that start at later time in the storm ( $t_0 > \tau_{crit}$ ) and at the rear ( $X_0 = 0$ ). For  
 177 this last situation, the initial group velocity of the waves must be larger or equal to  $V$ ,  
 178 otherwise those will not be able to propagate forward in the moving reference system and  
 179 will leave the storm from the rear (Figure 2 light-blue curves, defined as  $X(t, 0, t_0, V)$ ).

180 Characteristic curves for the three cases are separated by a special case correspond-  
 181 ing to the longest, most energetic characteristic curve (Figure 2, dark blue line). It de-  
 182 fines the largest generated wave energy for a given moving fetch and indicates if mov-  
 183 ing fetches are either "length-limited" or "time-limited". For length-limited conditions,  
 184 the most energetic waves leave the storm before it terminates, and the swell properties  
 185 are limited by the length scale of the storm (Figure 2a,b, green dot). For time-limited  
 186 conditions, the maximum swell energy is limited by the duration of the storm (Figure 2c).  
 187 For both cases, more than one characteristic curve is associated with the largest possi-  
 188 ble wave energy. Length-limited storms may last long enough such that more than one  
 189 curve reaches the front of the storm. This implies a constant radiation of energetic waves  
 190 from the front of the fetch, starting after a certain time from the onset of the storm (Fig-  
 191 ure 2a,b, green vertical lines). Time-limited cases may not last long enough for the curve  
 192 starting at  $X_{crit}$  to reach the front of the storm. These cases result in most energetic waves  
 193 leaving the storm in a spatial spread when it ends (Figure 2c, green horizontal line).

194 Extra-tropical storms can thus be either length- or time-limited (Figure 2b,c), while  
 195 tropical storms mostly correspond to length-limited wave growth regimes (Figure 2a, Kudryavt-  
 196 sev et al., 2015). To illustrate this expected variability of extra-tropical storms, the ef-  
 197 fect of changes in the length, speed, and wind forcing on the largest generated group ve-  
 198 locity along the longest characteristic curve is shown in Figure 3. For typical scales of  
 199 extra-tropical storms (Figure 3a, green line), the fetches can be either time- or length-

200 limited (Figure 3a, black line). It is also possible that small extra-tropical storms do not  
201 even reach the trapping condition, as indicated to the left of the the dashed black line  
202 in Figure 3b.

203 This constant-wind model outlines the general dynamics of swell generation un-  
204 der a moving storm and how its bulk spatio-temporal parameters affect the resulting swell  
205 systems. However, this conceptual model fails to explain why observed swell events have  
206 a clear temporal maximum (Figure 1b to e) that seems to originate from a very small  
207 source location (Munk, 1947). In addition, this model implies that the forcing is con-  
208 stant within the fetch area and discontinuous at its boundaries.

## 209 2.2 A Gaussian moving wind model

210 Hereafter, we relax the assumption of constant wind forcing to better represent the  
211 storm’s life cycle and to account for the fact that observed winds vary smoothly over space  
212 and time. We now describe the wind forcing  $u(X, t)$  in Equation (4) as a two-dimensional  
213 Gaussian function in space and time. This two-dimensional Gaussian moving fetch can  
214 be interpreted as representative of the wind patch typically established behind the cold  
215 front of a low-pressure system (Figure 4, gray shading) that travels with about the same  
216 translation velocity  $V$  as the storm (Figure 4 orange arrows). This fetch typically estab-  
217 lishes on the equator-ward side of the storm and is tightly linked to the storm life-cycle  
218 (Neiman & Shapiro, 1993; Schemm & Wernli, 2014; Schultz et al., 2018). Anticipating  
219 on the results of the observational analysis in section 3, we assume that the propagation  
220 direction of the fetch (Figure 4 orange arrows) is aligned with its dominant wind direc-  
221 tion (Figure 4 blue arrows) and hence also aligned with the direction of the generated  
222 waves.

223 The space-time Gaussian wind forcing is defined by a wind speed maximum,  $u_{max}$ ,  
224 a 95%-width, and a 95%-duration, while the 95% corresponds to  $\pm 2$  standard deviations  
225 of the Gaussian curve. Solutions of (Equation 4) for two typical extra-tropical storms  
226 are shown in figure 5 a and d. A storm with a 95%-fetch-width of 1000 km, a 95%-duration  
227 of 3.6 days and  $u_{max} = 10 \text{ m s}^{-1}$  shows characteristic curves similar to the length-limited  
228 case of constant winds (Figure 5a, Figure 2b). The major difference is that character-  
229 istic curves converge and cross near the storm’s leading edge, at the end of the storm’s  
230 lifecycle (Figure 5a, day 2.5 to 3). The convergence of characteristic curves in a focus

231 area results from the spatial gradients in the Gaussian wind forcing and does not appear  
232 with a constant, Heaviside-function wind forcing (section 2.1). Hence, any realistic storm,  
233 with local wind maximum and smooth wind distribution, will have spatial gradients and  
234 focus characteristic curves from different parts of the moving storm.

235 The convergence of the characteristic curves show a focusing of wave energy by the  
236 superposition of wave trains and the formation of a convergence region (Figure 5a,d).  
237 The convergence and crossing of curves indicate that sea states with different genera-  
238 tion histories (different paths of integration) propagate to the focal area and locally en-  
239 hance the total wave energy spectrum. Enhanced wave energy will lead to increased dis-  
240 sipation and more non-linear wave-wave interactions (S. Hasselmann & Hasselmann, 1985;  
241 Kudryavtsev et al., 2021), i.e. the convergence of wave energy can add another forcing  
242 term in Equation (4). The largest estimated wave energies on the characteristic curves  
243 (Figure 5b, light blue to green curves) are thus likely lower-bound estimates, because in-  
244 dependent solutions along the characteristics do not capture the expected enhanced dis-  
245 sipation and non-linear wave-wave interactions due to wave energy convergence. Still,  
246 the proposed model is useful to explain the governing relations between the fetch scales  
247 and the moving storm, although it might lead to systematic biases for the total wave en-  
248 ergies and peak wave frequencies.

249 The described wave-ray convergence leads to an area with significantly enhanced  
250 wave energy that can last for about half a day (Figure 5a between day 2-2.5 and Fig-  
251 ure 5d between day 2.5 and 3). This area encloses the steepest waves of the wave gen-  
252 eration process and is substantially smaller than the wind fetch that caused it (Figure 5a,d,  
253 gray shading). In the following, we argue that this small and distinct area acts as the  
254 source location for linearly propagating swell waves. From a distant location, it can be  
255 interpreted as a point source of swell waves (section 3.2, Munk, 1947). This source lo-  
256 cation corresponds to the transition region from a non-linear and very steep sea, mainly  
257 driven by wave-wave interactions, to a dominantly linear sea. In this transition region,  
258 the wind forcing decreases and subsequent wave-energy fluxes across frequencies vanish  
259 as well. The transition results in a linear sea that is dispersive and its wave energy starts  
260 to travel as the superposition of linear waves. This interpretation of the characteristic  
261 curves focusing in a transition region predicts that an observable source location of swell  
262 systems should be displaced ahead of the strongest moving winds, rather than at the the

263 center of the high wind speed region. Observational evidence for this phenomenon is shown  
 264 in section 3.

### 265 **2.3 Wave age of mature and old seas under moving fetches**

266 The Gaussian wind model emphasizes the non-linear behavior of the wave energy  
 267 growth and the importance of the wave field’s generation history under the moving wind  
 268 field. The wind forcing of sea states without a generation history can be solely described  
 269 by the local wave age  $\alpha = 2 c_g/u$  (right hand side of Equations 4), because the non-  
 270 linear advection term is small and  $c_g$  is proportional to  $u$  (Figure 5c and f day 0 to 2,  
 271 Edson et al., 2013). However, once non-linear advection increases, the wave energy growth  
 272 cannot simply be described by the local wave age parameter (Figure 5c and f day 2 to  
 273 3). These *mature* or *old seas* describe a situation where the simple relation between wave  
 274 age, group velocity, and wind speed breaks down. While the group velocity only slowly  
 275 grows, the wave age rapidly increases mainly due to constant or even decreasing local  
 276 wind speeds.

277 A comparable wind forcing  $u$  on the right-hand side of Equation (4) can thus cor-  
 278 respond to different degrees of wave development, i.e. different  $c_g$ . When waves start to  
 279 reach a mature state of development, the wind forcing starts to decrease and limit the  
 280 peak frequency downshift. We expect this non-linear behavior to be more important for  
 281 *old seas*, i.e. when the wave’s peak phase velocity and the local wind velocity approach  
 282 fully developed conditions of  $\alpha \simeq 0.85$  (P. Janssen, 2004). In addition, wave energy con-  
 283 vergence can counteract the local decay of the wind forcing and maintain a high wave  
 284 steepness (see previous section). These focusing effects, associated with converging wave  
 285 rays, should lead to enhancement and stabilization of the wave energy level. Thus, parametriza-  
 286 tions of the wave’s energy based on the local winds alone (e.g. Bourassa et al., 2013) may  
 287 fall short under moving fetches of synoptic storms. A proper description of the wave en-  
 288 ergy needs to account for the non-local wave dynamics.

### 289 **2.4 Scales of extra-tropical storms shape wave events**

290 The spatio-temporal scales of extra-tropical storms thus govern the focal point of  
 291 wave energy convergence and control resulting peak group velocities and wave energies.  
 292 Using the Gaussian wind model, the spatial gradients are proportional to the ratio of

293  $u_{max}$  and the 95%-width. Since the average storms width is related to the Rossby ra-  
294 dius and thus hard to change (Eady, 1949), the main control parameters become  $u_{max}$   
295 and  $V$ . To illustrate this resulting sensitivity on  $u_{max}$ , Figure 5d shows a moving fetch  
296 with the same parameters as in Figure 5a, but for a weaker peak wind speed and hence  
297 a weaker spatial gradient. Compared to strong wind conditions, weaker winds tempo-  
298 rally delay trapping condition  $c_g = V$  and the location where the characteristic curves  
299 cross (Figure 5a day 2-2.5 and b day 2.5 to 3) resulting in an over all lower group ve-  
300 locity.

301 A more systematic assessment is shown in Figure 6. Characteristic curves are cal-  
302 culated using Equation (4), but now for various combinations of storm sizes, duration,  
303 speeds, and wind forcing. For each set of storm conditions, we take the largest result-  
304 ing group velocities to test the sensitivity of  $c_g$  on the storm scales. Because character-  
305 istic curves converge and cross, wave energies merge, and the largest  $c_g$  derived from the  
306 method of characteristics is likely to be underestimated (section 2.2). However, this is  
307 still a useful metric to understand how the storm's scales control regimes of wave gen-  
308 eration.

309 Comparisons between the peak velocity  $u_{max}$  and translation velocity  $V$  for typ-  
310 ical scales of extra-tropical cyclones are shown in Figure 6a (95%-width and -duration  
311 are 1000 km and 3.5 days). The two cases from Figure 5 are indicated by black trian-  
312 gles and illustrate how solely changes in the peak wind speed lead to different peak wave  
313 energies. Higher peak velocities  $u_{max}$  or faster-moving storms  $V$  lead to higher group  
314 velocities (Figure 6a green shading). However, if a storm moves too fast, wave growth  
315 is limited because trapping effects are weaker or do not appear at all (Kudryavtsev et  
316 al., 2015, Figure 6a, to right of the black dashed line). No trapping occurs for fast storms  
317 with relatively weak winds; a situation that is likely uncommon for extra-tropical storms.

318 The fetch length and duration also affect the wave energy generation (Figure 6b).  
319 For typical but constant translation velocities and peak wind speeds, the wave energy  
320 increases when the storm is larger or lasts longer. However, more persistent storms are  
321 more effective in creating large wave energies than larger storms. For example, chang-  
322 ing the storm size by 20% from 1000 km to about 1200 km has a weaker effect than chang-  
323 ing the storm's duration by one day (Figure 6b, starting from the green dot). The im-

324 portance of the storm’s duration is again due to the trapping condition because trap-  
325 ping will always occur if the storm lasts long enough (section 2.1).

### 326 **3 A Case Study of a North Pacific Storm**

327 In this section, we combine observed surface wave spectra with reanalysis surface  
328 winds to assess the consistency of the Gaussian moving fetch model for swell generation.  
329 We analyse the case of a single storm over the North Pacific and explain how dispersed  
330 swell arrivals in wave buoy observations provide strong evidence for a small swell source  
331 location. We employ a physically constrained machine learning methodology that heav-  
332 ily borrows from ideas in Munk (1947); Barber and Ursell (1948); Snodgrass et al. (1966),  
333 as detailed in (Hell et al., 2019, 2020). This method triangulates the spatio-temporal co-  
334 ordinates of a single swell source which is simultaneously observed at five wave buoy sta-  
335 tions. This helps to check wherever or not the hypothesis from Kudryavtsev et al. (2015)  
336 can be extended to extra-tropical storms with smooth Gaussian winds (section 2, Fig-  
337 ure 4), and if the swell source location is indeed displaced compared to the strongest ob-  
338 served wind forcing. We first give a brief overview of the algorithm used to establish the  
339 source location. A more detailed description of the algorithm and two additional case  
340 studies can be found in the supplementary material T1 and figures F4 to F6).

#### 341 **3.1 Physically Constrained Optimization of a Parametric Swell Model** 342 **- In Brief**

343 We designed a parametric swell propagation model that is optimized on five pre-  
344 identified wave events. The spectral shape of the parametric model is described by a com-  
345 monly used shape function (K. Hasselmann et al., 1973; Elfouhaily et al., 1997), it’s time  
346 component as an Erlang distribution (Hell et al., 2019), and its decay as a function of  
347 the travel distance (Jiang et al., 2016, suppl. material T1.3).

348 The optimization is performed in five steps. First, swell wave events observed by  
349 the Coastal Data Information Program wave buoy network (CDIP, Behrens et al., 2019)  
350 are identified in the very long swell band. Second, the parametric model is fitted to each  
351 swell event at each wave buoy observation, and the uncertainty of its parameters are es-  
352 timated to evaluate the spectral dispersion slope and the quality of the observation (Hell  
353 et al., 2019). Third, the swell events are matched by their estimated initial time that can

354 be inferred from the events dispersion slope (Munk, 1947; Barber & Ursell, 1948; Snod-  
 355 grass et al., 1966; Collard et al., 2009). In the fourth step, these sets of matched swell  
 356 events are used to compare with parametric model outputs, but now assuming a com-  
 357 mon isentropic point source origin. Given a resulting hypothetical source point, the para-  
 358 metric model provides dispersion slopes, arrival times, and the wave’s amplitude atten-  
 359 uation for each member in the set of swell observations. A combined cost function is then  
 360 optimized for the common source point as described in the following (section 3.2).

361 The algorithm’s robustness largely builds from the fact that swell observations carry  
 362 information about their source location. The radial distance to a source location is in-  
 363 directly measured by the dispersion slopes of the wave events spectrograms (Munk, 1947;  
 364 Barber & Ursell, 1948; Snodgrass et al., 1966; Collard et al., 2009). The combination of  
 365 three or more buoy observations generally provides sufficient means to retrieve a com-  
 366 mon source location of the swell. Here we use observations at five locations to reduce  
 367 errors due to the spherical geometry and potential distorted observations at one or more  
 368 location (see next section). Details about this algorithm, the parametric swell model and  
 369 the cost-function design are given in the suppl. material T1.

### 370 **3.2 Triangulation of Swell Origins**

371 The cost function between the parametric model and the data helps to quantify  
 372 the performance of the model fit. A map in longitude, latitude and time of most likely  
 373 wave origins is derived to define a measure on the model fit. A likelihood  $L_{ef} = 1$  in-  
 374 dicates a perfect model fit and implies that all data variance is explained by the model,  
 375 while  $L_{ef} = 0$  indicates total model failure (Equation 11 in Supporting Information T1.5).

376 The result of the optimization is shown Figure 7 for a storm between the January  
 377 4th and 8th, 2016 (suppl. material F4 and F6 for other examples). The green hexagon  
 378 in Figure 7a indicates the most likely common source location for the swell events de-  
 379 tected at five buoys (Figs. 7b to f). The identified source location on January 4th, 2016  
 380 at 6:30 is identical for either a brute-force search in the parameter space, or a global cost  
 381 minimization (within a 25-km radius and 1 hour, suppl. material F1). Even though both  
 382 methods return a source location close to ocean station PAPA (CDIP 166), they some-  
 383 how lead to different interpretations of the process of swell generation. While the global  
 384 optimization returns a single optimum that would indicate a common point source for

385 the wave’s energy (Munk, 1947), the brute force method is in principle less precise but  
 386 can hint at multiple areas of similar likelihood. It samples a broader parameter space  
 387 and hence can provide a likelihood map of swell origins (Figure 7a green shading).

388 Note that the assumption of a single optimum essentially follows the idea of a lin-  
 389 ear inversion of the observed dispersion slopes in observations (Figure 1b to e, Figure 7b  
 390 to f, Munk, 1947), which in turn directly implies the existence of a point source (Fig-  
 391 ure 7a, green hexagon). However, the brute force method optimizes a cost function de-  
 392 signed under the assumption of this point source, but it returns a multitude of location  
 393 with similar likelihood (Figure 7a green shading). The assumption of an idealized point  
 394 source is still a reasonable interpretation for a single distant observer of swell, but some  
 395 refinement is needed in the context of the transient wave generation and decay (section 3.4).

396 The brute force sampling shows how the maximum of  $L_{ef}$  shifts in space for a se-  
 397 quence of time steps (Figure 7a green dots). It means that observed waves either orig-  
 398 inate earlier from a position west of the most likely source location, or later from a po-  
 399 sition east of the most likely source location (Figure 7a green dots). This trace of local  
 400 maxima in  $L_{ef}$  can be interpreted as a progression of wave origins rather than a single  
 401 point, as suggested by the constant or Gaussian wind models (Figure 2b,c, Figure 5).  
 402 This trace of local maxima in  $L_{ef}$  is used in the next section to combine the observed  
 403 wave events with observed wind patterns that are related to propagating storms.

404 Note that a successful optimization of the multi-station cost function may not al-  
 405 ways be straightforward. Indeed, local wind swell and wave-current interactions on the  
 406 swell travel paths are able to distort the wave buoys observations (Gallet & Young, 2014;  
 407 Villas Bôas et al., 2017), and possibly alter the optimization procedure (Hell et al., 2020).  
 408 Figure 7 b to f compares instances of the parametric wave model (colored contours) for  
 409 the most likely source location (green hexagon in panel a) to the respective observations  
 410 (colored shading). The parametric model captures the observed dispersion slopes in four  
 411 out of five cases. Comparison between the model and data from CDIP 106, close to Hawaii  
 412 (Figure 7e and red dot in Figure 7a), indicates a modeled wave arrival about one day  
 413 later and further away than the observation. Hence, the observed wave event close to  
 414 Hawaii could result from a closer source than suggested by the best model fit, and still  
 415 be related to the same storm system. In such a case, a different growth history, i.e. a  
 416 different effective fetch, would be necessary. This case study shows that a more holis-

417 tic understanding of the optimization hints at the complexity of wave generation in the  
 418 real world, but also shows that even imperfect and distorted data can support the hy-  
 419 pothesis in section 2.2.

### 420 **3.3 Comparing observed swell origins to reanalysis winds**

421 To interpret the relation between possible wave origins and the wind pattern that  
 422 creates them, we show three snapshots of surface winds and sea level pressure from hourly  
 423 ERA5 reanalysis on a  $0.25^\circ$ -grid in the North East Pacific (Figure 8, European Centre  
 424 for Medium-Range Weather Forecasts fifth-generation reanalysis for the global climate  
 425 and weather (CDS), 2017). The storm propagates eastward, and its associated strong  
 426 surface winds, the fetch, move eastward as well (red area at about  $160^\circ\text{W}$  and  $40^\circ\text{N}$  in  
 427 Figure 8a moves to about  $150^\circ\text{W}$  and  $50^\circ\text{N}$  in Figure 8c). The same propagation can  
 428 be seen for the local maxima of  $L_{ef}$  and hence for the source location of swell (Figure 7a  
 429 green dots). Interestingly, the swell origins appear systematically ahead of the highest  
 430 wind speeds (Figure 8a,b,c). This displacement between the swell origins, estimated from  
 431 wave buoys, and the highest wind forcing, estimated from reanalysis, is the same as pre-  
 432 dicted for swell generation by a moving fetch (section 2.2). Hence the physically informed  
 433 brute-force optimization shows how the trace of most likely swell origins, i.e. a trace in  
 434 the local maximum of  $L_{ef}$ , co-travels with the patch of highest wind speeds under a mov-  
 435 ing storm.

### 436 **3.4 Computing waves growth from realistic moving winds**

437 We can now compare the propagating, co-located winds patches and swell origins  
 438 to the moving Gaussian wind model. To do so, we transform the surface winds in a La-  
 439 grangian frame using its average propagation speed.

440 We first define a transect line for the wind data using a least-square fit to the trace  
 441 of  $L_{ef}$  (Figure 8 a to c, straight black lines between A and B). Next, we take data along  
 442 this transect over a width of 440km from the wind reanalysis between the points A and  
 443 B. The wind is rotated to along- and across- transect velocities and then averaged or-  
 444 thogonal to the transect (suppl. material F2). The resulting time evolution of the along-  
 445 and across-track averaged winds as well as contours of  $L_{ef}$  are shown in Figure 8 d and  
 446 e. Finally, we estimate the average propagation speed  $V$  of the along-transect wind patch

447 using again a least square fit (Figure 8d and e, black sloped line, suppl. material F3).  
 448 The estimated propagation speed  $V$  of  $14.1 \text{ m s}^{-1}$ s then used to shift the data in the frame  
 449 of reference of the moving wind patch.

450 The resulting along-transect velocities and the contours of  $L_{ef}$  are shown in the  
 451 moving frame of reference in figure 9a. The area of most likely swell origin is clearly dis-  
 452 placed in space and time compared to the highest wind speeds (Figure 9a green contours  
 453 and red shading). The most likely swell origin is about one day delayed compared to the  
 454 strongest winds. It is thus unlikely that the observed swell waves originate from the area  
 455 of highest wind speeds. Instead, swell waves are delayed in the moving frame of refer-  
 456 ence. A temporal delay in the moving frame implies also a spatial displacement in the  
 457 Eulerian frame, as already observed in Figure 8. This space-time displacement cannot  
 458 be explained by the stationary fetch laws, which only describe swell properties away from  
 459 a constant-wind “fetch” area (section 2 Kitaigorodskii, 1962; K. Hasselmann et al., 1973;  
 460 Elfouhaily et al., 1997). This space-time displacement is in line with the predicted de-  
 461 lay in the moving frame of reference between strongest wave growth and linear swell prop-  
 462 agation dispersion (section 2.2).

463 The spatial-temporal delay of the estimated wave origins can be explained by analysing  
 464 the characteristic curves of wave growth forced with the transformed wind data. As in  
 465 section 2.2, we use the method of characteristics to solve Equation (4) but now using the  
 466 along-transect reanalysis winds in the moving frame of reference (Figure 9a and b shad-  
 467 ing). The characteristic curves are initialized from a sea at rest ( $\omega_p \approx 20 \pi \text{ s}^{-1}$ , Appendix  
 468 A) where the winds are zero ( $u = 0$ ) and represent paths of wave energy growth that  
 469 propagate in the moving reference frame (Figure 9b black and blue contours). As in the  
 470 idealized model (section 2.2), the line thickness shows that wave energy and group ve-  
 471 locity increase along the path while  $\omega_p$  decreases. Several characteristic curves reach the  
 472 trapping condition ( $V = c_g$ ) and some paths converge and cross due to large-scale gra-  
 473 dents in the wind forcing (Figure 9b, day 2.5-3.5, see also supp. Figure F5 for another  
 474 case study).

475 The path with the largest final wave energy is shown in blue in figure 9b. This char-  
 476 acteristic curve is terminated, where the wind forcing reaches zero (Figure 9b, green hexagon),  
 477 indicating the last space-time location of possible active wave growth. While this is a  
 478 practical definition of where wave growth decays, because Equation 4 only captures wave

479 growth, it is remarkable that the longest characteristic curve overlaps with the area of  
480 most likely swell origin and crosses its peak (Figure 9b, green dot and contours). Even  
481 though this area of most likely origins is transformed in the moving frame of reference,  
482 it is derived independently from the solutions of the characteristic curves. And, while  
483 the wind forcing of the characteristic curves is taken along the trace of the triangulated  
484 swell origins (section 3.2), there is no need for the longest characteristic curve to match  
485 the independent buoy observation. This match between the forward calculation of the  
486 wave growth model forced by reanalysis winds (Equation 4) and the back triangulation  
487 of linear swell propagation (Figure 7) provides evidence that the conceptual idea of a Gaus-  
488 sian wind model (section 2.2) is sufficient to capture the necessary dynamics of wave growth  
489 and swell generation by a moving storm. This is, to some extent, surprising given the  
490 non-linear nature of Equation 4 and potential biases in the surface winds (Gille, 2005;  
491 Wentz et al., 2015; Ribal & Young, 2019; Trindade et al., 2020; Allen et al., 2020; Hell  
492 et al., 2020).

493 To further explain why wave growth from transformed reanalysis winds is able to  
494 match the triangulated swell origins, we use the Gaussian wind model from section 2.2,  
495 for parameters that match the scales of the observed wind forcing ( $V = 14.1 \text{ m s}^{-1}$ ,  
496  $u_{max} = 22 \text{ m s}^{-1}$ , a 95%-duration of 4 days and 95%-width of 2800 km, Figure 9c). The  
497 Gaussian wind model is able to reproduce and predict a trajectory of the largest wave  
498 energy align with the observed source locations (compare Figure 9b,c blue line and green  
499 dot). It captures the observed larger-scale spatial and temporal wind gradients that are  
500 needed to create the convergence of the characteristic curves (Figure 9 b and c). This  
501 provides evidence that a Gaussian moving fetch is a sufficient model to understand swell  
502 generation by extra-tropical cyclones (see supplementary material F4 to F6 for additional  
503 examples).

#### 504 **4 Discussion and Conclusion**

505 Swell wave generation from extra-tropical storms is a long-standing problem (Munk,  
506 1947). Here, we presented a comprehensive explanation of why swell systems likely orig-  
507 inate from small locations that do not necessarily match the high wind forcing regions.  
508 This explanation points to aspects in the process of swell generation that need to be bet-  
509 ter captured to improve wave forecast models but are also relevant for estimating air-  
510 sea fluxes and ocean mixed-layer variability.

511 A two-dimensional Gaussian wind model is found to be sufficient to represent the  
 512 wave generation under a moving storm and to improve upon constant wind forcing con-  
 513 ditions (sections 2.1 and 2.2). The storm and its cold sector are assumed to travel with  
 514 a constant translation velocity (Figure 4), even though in reality, the storm’s fetch prop-  
 515 agation might likely vary in speed and direction. The proposed model is highly ideal-  
 516 ized but is still detailed enough to capture the main wave-generation mechanism dur-  
 517 ing the life-cycle of an extra-tropical storm as for example described in Neiman and Shapiro  
 518 (1993), Neiman et al. (1993), Schemm and Wernli (2014), and Schultz et al. (2018). It  
 519 is also found to be a sufficient minimal model to explain observed displacements of es-  
 520 timated swell source location compared to the highest wind forcing locations (section 3.3,  
 521 Figure 9b and c, Hell et al., 2020). The combination of a Lagrangian wave-growth model  
 522 with an optimized swell propagation model suggests three stages in the life cycle of swell  
 523 wave energy:

524 • **Stage 1: Wave growth under a moving fetch in a young and growing sea**

525 Starting from a sea at rest, wind forcing creates short waves as a result of wave-  
 526 wave interactions, wave growth and dissipation. Wave-wave interactions lead to  
 527 a continuous decrease of the peak frequency  $\omega_p$ , while the total wave’s energy and  
 528 significant wave height increase (Equation 3). For an actively growing wave field,  
 529 the wave energies in different frequency bands are strongly coupled through wave-  
 530 wave interactions. This coupling likely inhibits frequency dispersion and let us uniquely  
 531 describe the wave spectra by its peak parameters. The energy of the non-linear  
 532 sea state thus mainly travels with the group velocity of its dominant frequency  
 533  $c_g(\omega_p)$  shown by characteristic curves in Figure 10.

534 At first, waves are slower than the storm and propagate backwards in the mov-  
 535 ing frame of reference. With time this *young sea* continues to grow, its peak fre-  
 536 quency decreases, and the associated group velocity accelerates (Figure 10). Even-  
 537 tually, the wave’s energy starts to propagate with a speed comparable to the storm,  
 538 such that the wave energy is trapped under the storm ( $c_g = V$ , section 2.1). The  
 539 wave’s energy is now strongly growing because the previously established non-linear  
 540 sea is exposed to the strongest winds of the moving fetch (*growing sea* in the cen-  
 541 ter of Figure 10). This process ends when the wave energy leaves the storm or when  
 542 the wind forcing vanishes.

543 This strong wave energy growth depends on if the wave’s energy is trapped ( $c_g =$   
 544  $V$ ) or not. This trapping, or quasi resonance (Dysthe & Harbitz, 1987; Young, 1988;  
 545 Bowyer & MacAfee, 2005; Young & Vinoth, 2013; Kudryavtsev et al., 2015), mainly  
 546 depends on the ratio of the wind speed to the translation velocity (Equation 5 and  
 547 6). Wave energy is more easily trapped if the translation velocity of the storm is  
 548 small or the wind speed is high (Figure 3b and 6a).

549 • **Stage 2: Decay of non-linear terms in an old sea**

550 When the wind forcing decays, the wave energy does not immediately turn into  
 551 linearly propagating swell. Instead, dissipation may remain active, with the wave-  
 552 wave interactions counteracting the wind forcing decay. The peak frequency down-  
 553 shift ceases and the waves’s steepness starts to decrease. Hence, the still steep non-  
 554 linear sea decays (Kudryavtsev et al., 2021). This results in a transformation to  
 555 progressively more linear sea (*old sea*, Figure 10). Timescales on which the non-  
 556 linear terms in the wave-action equation decay are inversely proportional to the  
 557 fourth power of the wave steepness and are typically about three hours (Zakharov  
 558 & Badulin, 2011; Zakharov et al., 2019). During this time, the wave field trans-  
 559 forms from a non-linear (steep wave spectrum) to a dominantly linear sea state  
 560 (broader wave spectrum). Because the wave field still propagates during this re-  
 561 laxation time, the location where the wave spectrum is dominantly linear differs  
 562 from the last location where the wind was still substantially growing waves.

563 • **Stage 3: Linear propagation of swell**

564 Once the wave field becomes linear, the wave energy in each frequency band prop-  
 565 agates following the deep water wave dispersion relation as a *linear sea* (Figure 10  
 566 and radial propagation in Figure4). At this stage, almost no interaction occurs  
 567 between the different frequency bands. From this point on, the travel distance and  
 568 energy attenuation are proportional to the amount of dispersion, which in turn  
 569 is the difference in the arrival time between waves of different frequencies (suppl.  
 570 material T1.4, Munk, 1947; Barber & Ursell, 1948; Ardhuin et al., 2009). A back-  
 571 ward triangulation based on linear propagation as in section 3 can then be applied  
 572 successfully, as long as the swell’s interactions with currents, eddies, and other wind  
 573 forcing remain weak along its great circle path.

574 The Gaussian wind model is a smooth forcing field that can also be related to the  
575 scales of extra-tropical storms (Figure 6 and 11). Four parameters characterize the mov-  
576 ing fetch; its translation velocity  $V$ , its length-scale along the peak wind direction (95%-  
577 width), its lifetime (95%-duration), and its peak wind speed  $u_{max}$ . All of them are de-  
578 termined by synoptic-scale dynamics. It follows that processes that influence the storm's  
579 intensity may also influence the shape, amplitude, and peak period of the observed swell  
580 events (Figure 11). This analysis provides a practical means to connect observed swell  
581 events to storm characteristics and confirms that non-local swell measurements can be  
582 used to quantify storms over the open ocean (Hell et al., 2020). This can further link the  
583 current and future swell wave climate to common diagnostics of extra-tropical storms  
584 (Figure 11, Schultz et al., 2018; Hoskins et al., 1985; Schemm & Wernli, 2014) and their  
585 statistics (Charney, 1947; Eady, 1949; Andrews & McIntyre, 1976; Bengtsson et al., 2006;  
586 Mbengue & Schneider, 2016; Shaw et al., 2016, and others)

587 The idealized model of a moving fetch suggests that wave event intensities are most  
588 sensitive to spatial gradients in the wind forcing fields (Figure 6a). Since the average size  
589 of storms, and their fetch (1000 km), are constrained by basic properties of Earth's mid-  
590 latitudes flow (Eady, 1949; Bengtsson et al., 2009; Hodges et al., 2011; Catto, 2018; Sin-  
591 clair et al., 2020), the spatial wind gradient is mainly determined by the peak wind speed  
592  $u_{max}$ . A larger peak wind speed and a stronger spatial wind gradient lead to more ef-  
593 ficient trapping of the wave energy, with the consequence of larger swell waves. Note that  
594 at the leading edge of the moving fetch, the spatial wind gradient is related to the com-  
595 plex dynamics at the storm's cold front. The Gaussian wind model (section 2.2) may not  
596 fully capture these smaller-scale wind gradients but can be easily extended by introduc-  
597 ing non-Gaussian corrections to the spatial wind distribution.

598 Intensities of wave events are also sensitive to the ratio of the peak wind speed  $u_{max}$   
599 and storm propagation speed  $V$  because they are key to determine the trapping condi-  
600 tions (Equation 6). If their ratio,  $u_{max}/V$ , is relatively large, the trapped wave energy  
601 leaves the wind forcing at its leading edge, co-located with the storm's cold front (Fig-  
602 ure 4 and Figure 7e). This can be interpreted as a "length-limited" fetch (Figure 2b and  
603 Figure 5a). In contrast, if  $u_{max}/V$  is small the trapping is less intense and the wind forc-  
604 ing may decay before the wave energy reaches the leading edge of the fetch. This is bet-  
605 ter interpreted as a "time-limited" fetch (Figure 2c, Figure 5d). Length- or time-limited  
606 fetches may frequently occur under extra-tropical storms (Figure 3, 6, and 11), while trop-

607 ical storms usually reach a length-limited situation that constantly radiates waves (Fig-  
608 ure 2a). Under such a condition, the generated wave field would depend only on the storm's  
609 propagation velocity (Kudryavtsev et al., 2015).

610 Reanalysis products have biases in their representation of wind extremes (Gille, 2005;  
611 Hell et al., 2021). These wind extremes are represented in the Gaussian model as the peak  
612 wind speed. The sensitivity of the resulting swell peak period to the peak wind speed  
613 (section 2.4) indicates that biases in wind extremes can cause biases in wave models by  
614 altering the processes of wave growth (Aouf et al., 2021). Errors in the peak wind speed  
615 of a few meters per second change the spatial wind gradients, alter the location of the  
616 highest energy convergence, and consequently the location where the swell energy starts  
617 to travel as linear waves. This might result in biases in arrival times of swell events. The  
618 present analysis suggests that swell analysis will lead to a better representation of ex-  
619 treme surface wind speeds and hence also improve surface wave models (Cavaleri, 2009;  
620 Cardone et al., 1996; Ponce & Ocampo-Torres, 1998; Feng et al., 2006; Durrant et al.,  
621 2013; Stopa & Cheung, 2014; P. A. Janssen & Bidlot, 2018; Osinski & Radtke, 2020).

622 Any moving fetch with non-constant winds will have spatial wind gradients lead-  
623 ing to convergence of wave energy (section 2.2). A convergence of the characteristic curves  
624 from different regions of the moving fetch can create wave-energy hot spots, indicated  
625 by crossing characteristic curves (Figure 5). This convergence of wave energy may lead  
626 to additional dissipation and/or additional wave-wave interactions, which intensify swell  
627 wave growth and the down-shifting of the peak frequency. Hence, it could be modelled  
628 as another forcing term in Equation 4, to which the wave spectrum can adjust rather  
629 quickly. It also implies that these local wave energy convergences correspond to enhanced  
630 breaking, which dissipates part of the wave energy in the upper ocean. Accordingly, we  
631 speculate that the location of the strongest winds may not necessarily be the location  
632 of the largest momentum transfers to the ocean, nor the location of the observable ori-  
633 gin of swell (Figure 4). Instead, swell source locations can be interpreted as markers for  
634 intense momentum flux from the wave field to the ocean.

635 Finally, air-sea fluxes of heat, momentum, and CO<sub>2</sub> are currently parameterized  
636 by the standard bulk flux formulae (Fairall et al., 2003; Edson et al., 2013). The wave  
637 field's contribution to these fluxes is often described by wave age  $\alpha = 2u c_g^{-1}$ . We sug-  
638 gest that the sea state at many locations under a moving storm cannot be explained solely

639 by local parameters, like wave age (Figure 5 c and f). Because the local sea state results  
640 from the moving wind fetch, its group velocity is constrained by wind forcing to which  
641 the wave energy was previously exposed. This introduces a non-local condition on the  
642 momentum transfer between the atmosphere and ocean. This means that feedbacks be-  
643 tween the wave spectrum and the turbulent spectrum of the atmosphere (Ayet et al., 2020;  
644 Zou et al., 2020), or feedbacks of surface waves and the upper ocean (Li et al., 2016, 2019),  
645 can only capture these wave-induced non-local conditions when the wave spectra are com-  
646 puted, i.e. advected, rather than assumed by local conditions. Alternatively, the wave  
647 spectra could be characterised by metrics that account for non-local wave history that  
648 goes beyond wave age.

649 Here we have used standard wave buoy observations of ocean swell in the eastern  
650 Pacific to identify storm systems that generate wave events. We defined a parametric  
651 swell model that combines standard swell spectra, a prescribed time decay, and the deep  
652 water wave dispersion (suppl. Material T1). The novelty in this approach is that swell  
653 events from storms are treated as objects whose shapes and origins are learned from the  
654 data. This allows us to a) reevaluate common models of wave spectra, b) classify and  
655 match swell observations in a diverse set of existing data sets, and c) use deviation from  
656 this parametric model to learn about other phenomena, for example wave-current inter-  
657 action (Gallet & Young, 2014; Villas Bôas & Young, 2020; Quilfen & Chapron, 2019).

658 We have outlined how choices in the design of a supervised learning algorithm are  
659 linked to the understanding of the physics we wish to investigate. Wave generation is  
660 a stochastic process that involves non-linear physics, such that a single point source of  
661 swell is not realistic, even though it is assumed in the parametric model (section 3.2, suppl.  
662 Material T1). We account for this paradox by letting the optimization be imprecise (brute-  
663 force method), rather than precise (global optimization). The latter would likely over-  
664 fit the model, which could be corrected by an extensive posterior uncertainty exploration  
665 around a prior defined optimum. In either case, imprecise optimization and uncertainty  
666 estimates of the most likely swell origins play an important part in this analysis (Fig-  
667 ure 7). This approach suggests that observed swell arrivals could be modeled by a su-  
668 perposition of swell source points using ordinary fetch laws and Green's functions along  
669 the trace (Fig. 7a, green dots). However, that kind of model would still fall short in de-  
670 scribing the non-linear dynamics prior the linear swell propagation (section 2).

671 **Appendix A Solution of the Lagrangian advection equation in the  $(X, t)$**   
 672 **plane**

673 **A1 Method of characteristics for constant wind forcing**

674 We follow Kudryavtsev et al. (2015) and solve the advection equation Equation (4)  
 675 in the moving frame of reference for constant winds  $u$ , a constant advection speed  $V$  along  
 676 a characteristic line  $(t(s), X(s), c_g(s))$ , and with initial conditions  $t_0, X(t_0)$  and  $c_g(t_0)$   
 677 at  $s = 0$ . The set of equations to be solved is

$$\frac{dt}{ds} = 1 \tag{A1}$$

$$\frac{d\omega_p}{ds} = \left(\frac{g}{u}\right)^2 \phi(\alpha) \tag{A2}$$

$$\frac{dX}{ds} = c_g - V, \tag{A3}$$

678 where the peak period  $\omega_p$  is related to the peak group velocity via the deep water dis-  
 679 persion relation  $c_g = \frac{1}{2} \frac{g}{\omega_p}$ . The equations A1 to A3 are solved numerically in section  
 680 2.2 and there after. The characteristics curves are initialized for numerical reason the  
 681 from  $\omega_p \approx 20 \pi \text{ s}^{-1}$ . This corresponds to  $c_g$  of about  $7.8 \times 10^{-2} \text{ m s}^{-1}$  and its differ-  
 682 ence from zero has no effects on the overall results.

Equation (A1) reduces to  $s = t - t_0$  and hence gives the characteristic coordi-  
 nate as a function of time. Equation (A2) is the temporal fetch relation which reads in  
 dimensional coordinates

$$\omega_p(t) = c_{\alpha t} \frac{g}{u} \left(\frac{g}{u}\right)^{q_t} (t - t_0)^{q_t} + C_{\omega}, \tag{A4}$$

with  $C_{\omega}$  is the integration constant, and  $q_t$  and  $c_{\alpha}$  are defined in appendix A3 or Kudryavtsev  
 et al. (2015). Equation (A2) can also be solved for the group velocity  $c_g$ , and yields

$$c_g(t) = c_{\tau}^{q_t} u \left(\frac{g}{u}\right)^{-q_t} (t - t_0)^{-q_t} + c_g(t_0). \tag{A5}$$

with  $c_{\tau}$  again defined in appendix A3. Finally, the position  $X$  along the characteristic  
 reads, from equation (A3)

$$X(t) = \frac{1}{-q_t + 1} c_{\tau}^{q_t} u \left(\frac{g}{u}\right)^{-q_t} (t - t_0)^{-q_t + 1} + (t - t_0)[c_g(t_0) - V] + X(t_0). \tag{A6}$$

683 **A2 Derivation of the critical time and length scale for constant mov-**  
 684 **ing wind forcing**

685 Waves generated at the beginning of the storm ( $t_0 = 0$ ) follow characteristic curves  
 686 with initial conditions  $X(0) = X_0$  and  $c_g(0) = 0$ , assuming the sea initially at rest.

The time scale  $t_{crit}$  at which the trapping of wave every appears is when Equation (A5) equals the speed of the storm  $V$ , such that

$$V = c_{\tau}^{q_t} u \left(\frac{g}{u}\right)^{-q_t} t_{crit}^{-q_t}, \tag{A7}$$

which yields

$$t_{crit} = \frac{c_{\tau}}{g} u^{-q} V^{1+\frac{1}{q}}. \tag{A8}$$

At  $t_{crit}$ , waves that have started at  $X_{crit}$  should be exactly at the rear boundary of the storm, i.e. at  $X = 0$ . From equation (A6), this yields

$$X_{crit} = \frac{-1}{-q_t + 1} c_{\tau}^{q_t} u \left(\frac{g}{u}\right)^{-q_t} t_{crit}^{-q_t+1} + t_{crit} V, \tag{A9}$$

$$X_{crit} = \frac{c_{\tau}}{g} u^{1+\frac{1}{q_t}} V^{1-\frac{1}{q_t}} \left[ \frac{q_t}{1-q_t} \right], \tag{A10}$$

$$X_{crit} = \frac{c_{\tau}}{g} q u^2 \left(\frac{u}{V}\right)^{\frac{1}{q}}, \tag{A11}$$

687 with using Equation (A8) and  $q_t$  defined in Equation (A13). Waves with an initial con-  
 688 dition  $X_0 > X_{crit}$  will eventually move faster than the storm and will all have the same  
 689 group velocity at a given time, following the temporal fetch law Equation (A5).

690 **A3 Choice of constants**

Wave growth estimated by the Lagrangian advection equation (Equation 4) and subsequent quantities depend on a set of semi-empirical parameters (Badulin et al., 2007). Here we choose parameters based on K. Hasselmann et al. (1976), for the case of a “young sea”. With the choice of  $q = -3/10$  and a wave growth parameter  $c_{\alpha} = 15.4$ , the other parameters follow as

$$p = -5q - \frac{1}{2} = 1, \tag{A12}$$

$$q_t = \frac{q}{1+q} = -0.43, \tag{A13}$$

$$c_{\alpha t} = \left[ c_{\alpha}^{\frac{1}{q}} \frac{1+q}{2} \right]^{q_t} \approx 76.08, \tag{A14}$$

$$c_e \approx 4.41 \times 10^{-7}, \tag{A15}$$

and

$$c_{\tau} = 2^{(1-\frac{1}{q_t})} c_{\alpha}^{-\frac{1}{q}} (1+q)^{-1} \approx 1.23 \times 10^5. \tag{A16}$$

691 Note that, Kudryavtsev et al. (2015) used a slightly different  $q$  (see their appendix A1),  
 692 but the results are comparable.

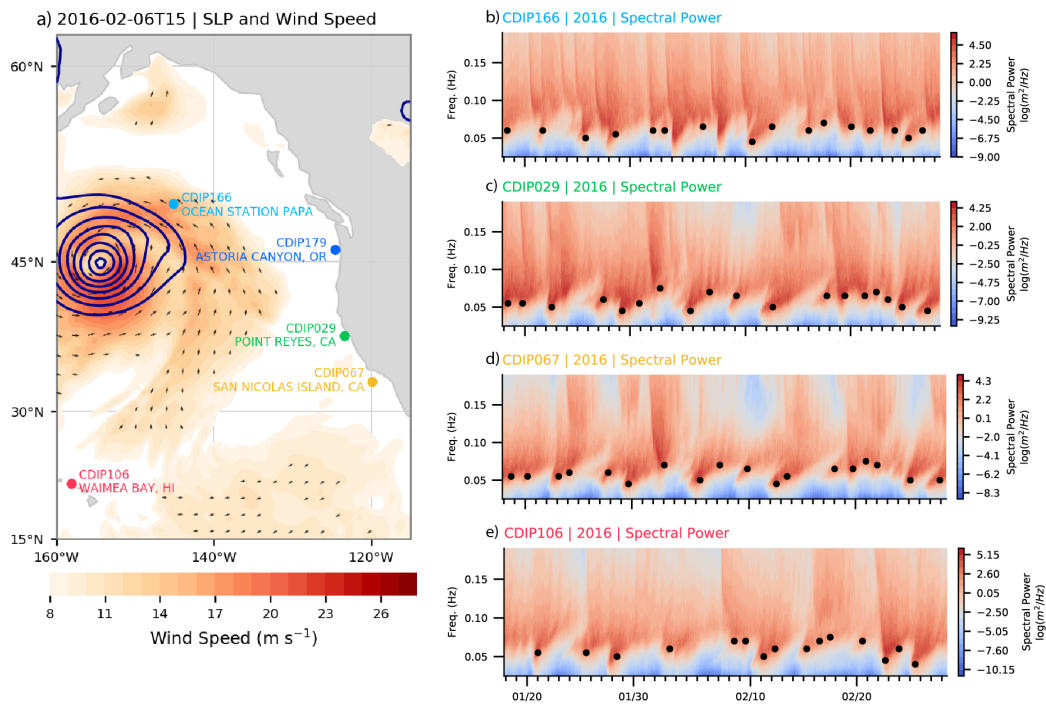


**Figure 1.** a) Example synoptic situation on February 2nd, 2016 with the surface wind speed (shading) and negative anomalies of Sea level Pressure (SLP) in dark blue with 5 hPa increments. The arrows indicate the surface wind direction and intensity. The position of the CDIP wave buoy stations in panel b to e are shown as colored dots. The 10-meter winds and SLP fields are taken from the hourly ERA5 analysis on a 0.25 °-grid (European Centre for Medium-Range Weather Forecasts fifth-generation reanalysis for the global climate and weather (CDS), 2017). (b to e) Observed spectrograms between mid-January and mid-February 2016 for CDIP029, CDIP067, CDIP106 and CDIP166 (Behrens et al., 2019). The black dots indicate individual swell events identified by their long-period forerunner (suppl. material T1).

693 **Acknowledgments**

694 The CDIP data is available on the wave buoy observations were furnished by the Coastal  
 695 Data Information Program (CDIP, <https://doi.org/10.18437/C7WC72>), Integrative Oceanog-  
 696 raphy Division, operated by the Scripps Institution of Oceanography, under the spon-  
 697 sorship of the U.S. Army Corps of Engineers and the California Department of Parks  
 698 and Recreation. The ERA5 reanalysis was provided through the through the Coperni-  
 699 cus Climate Change Service Climate Data Store (CDS, <https://doi.org/10.24381/cds.adbb2d47>)  
 700 in 2017. Neither the European Commission nor ECMWF is responsible for any use that  
 701 may be made of the Copernicus information or data it contains.

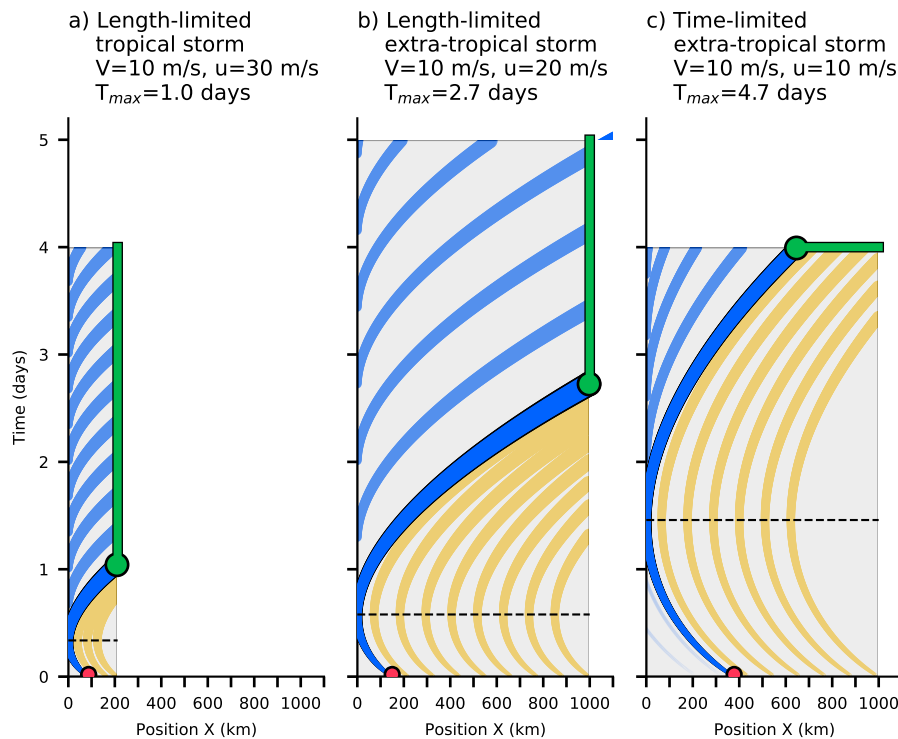


**Figure 2.** Characteristic wave energy curves for an idealized fetch model with constant and translating wind. a) Characteristic curves for typical scales of a tropical cyclone ( $V = 10 \text{ m s}^{-1}$ ,  $u = 30 \text{ m s}^{-1}$ , duration  $T = 4$  days, length scale is 200 km, same parameters as in Kudryavtsev et al., 2015). The characteristic curves with lowest  $\omega_p$  and the highest wave energy, i.e. the longest characteristic curve (dark blue) start at the red dot ( $X_{crit}$ ) and goes to its exit location (green dot). The green line indicates exit locations that have the same value of  $\omega_p$  as the green dot, but in this case the wave energy was generated along the light blue lines starting after  $\tau_{crit}$  (dashed black line). Orange lines indicate characteristic curves that start at  $t_0$  but don't grow as long as the longest characteristic curve and result in smaller wave energy. The thickness of the characteristic curves is proportional to the wave's energy, or  $\omega_p^{-1}$ . b) Same as a) but for a length-limited extra-tropical storm with strong winds ( $V = 10 \text{ m s}^{-1}$ ,  $u = 20 \text{ m s}^{-1}$ , duration  $T = 5$  days, length scale is 1000 km). c) Same as b) but for a time-limited extra-tropical storm with weak winds  $u = 10 \text{ m s}^{-1}$ .

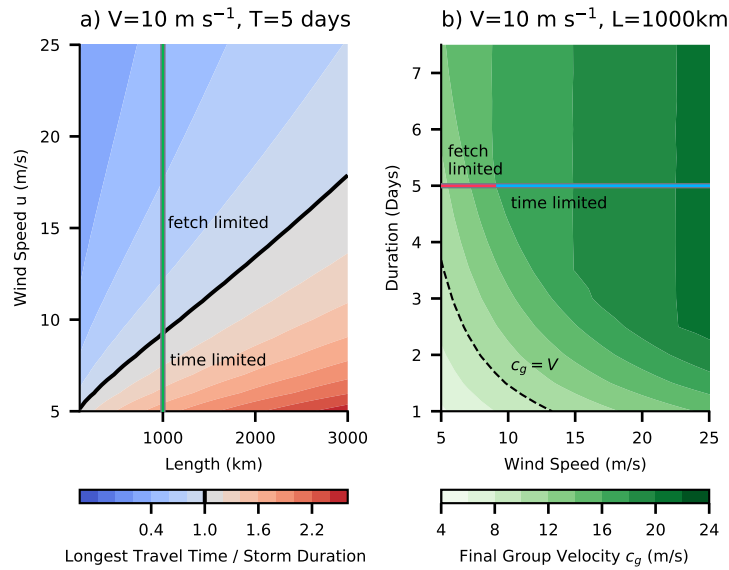


**Figure 3.** a) Travel time of the longest characteristic divided by the fetch duration (5 days) for constant moving wind model with a propagation speed  $V=10 \text{ m s}^{-1}$  (as in Figure 2b,c). Blue shading indicates length-limited fetches, red shading indicates time-limited fetches and the black line shows cases with a travel time along the longest characteristic curve equal to the duration of the fetch. The green line indicates the parameter space in b). b) Group velocity of the longest characteristic curves of fetches with  $L=1000 \text{ km}$ , translational speed of  $V=10 \text{ m s}^{-1}$ , but varying wind speed and duration. The trapping condition ( $c_g = V$ ) is shown as black dashed line, while the fetch- and time-limited cases are shown as red and blue lines.

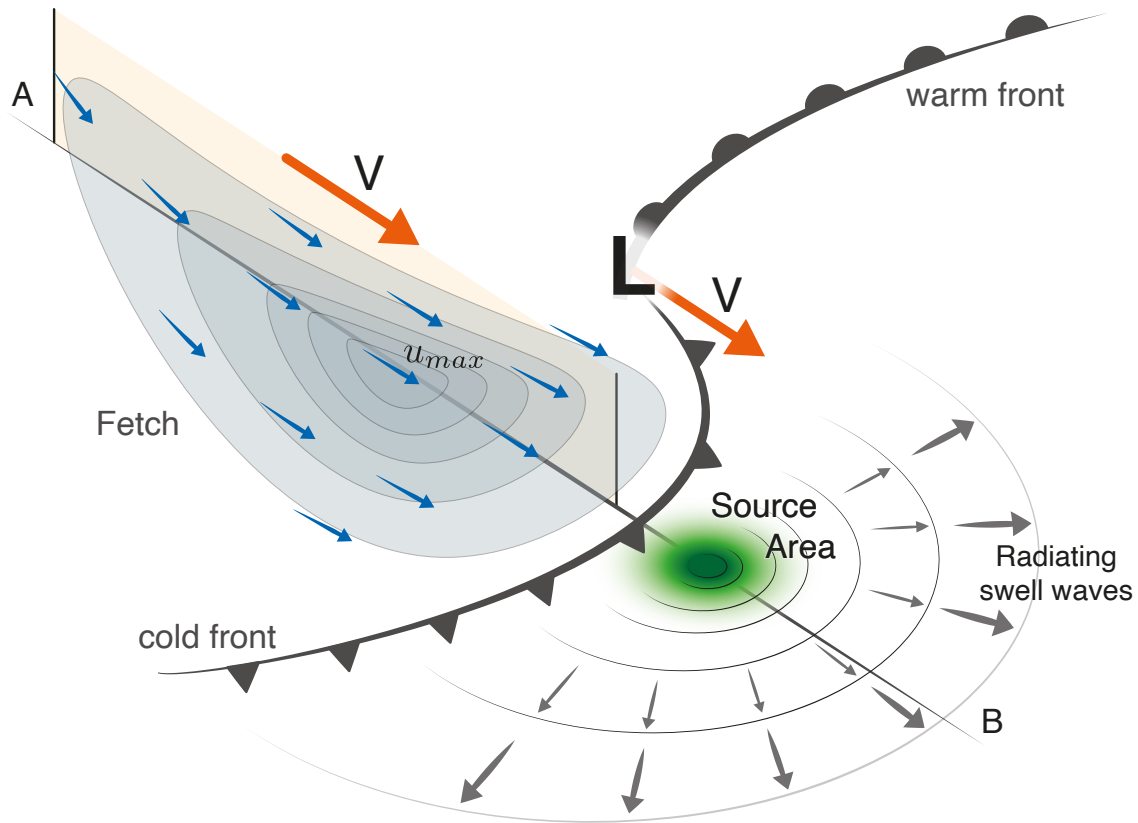


**Figure 4.** A moving fetch embedded in an Northern Hemisphere extra-tropical storm. The storm's center  $L$  is adjacent by a warm and cold front (thick gray lines with half circles or triangles). The moving fetch is located behind the cold front (gray shading with blue arrows) and moves with the same translational velocity  $V$  as the cyclone center  $L$  (orange arrows) to the bottom right. The green area indicated the source region as suggested by a Gaussian moving wind model (section 2.2) and observations (section 3). Swell waves radiate away from this source region (small gray arrows).

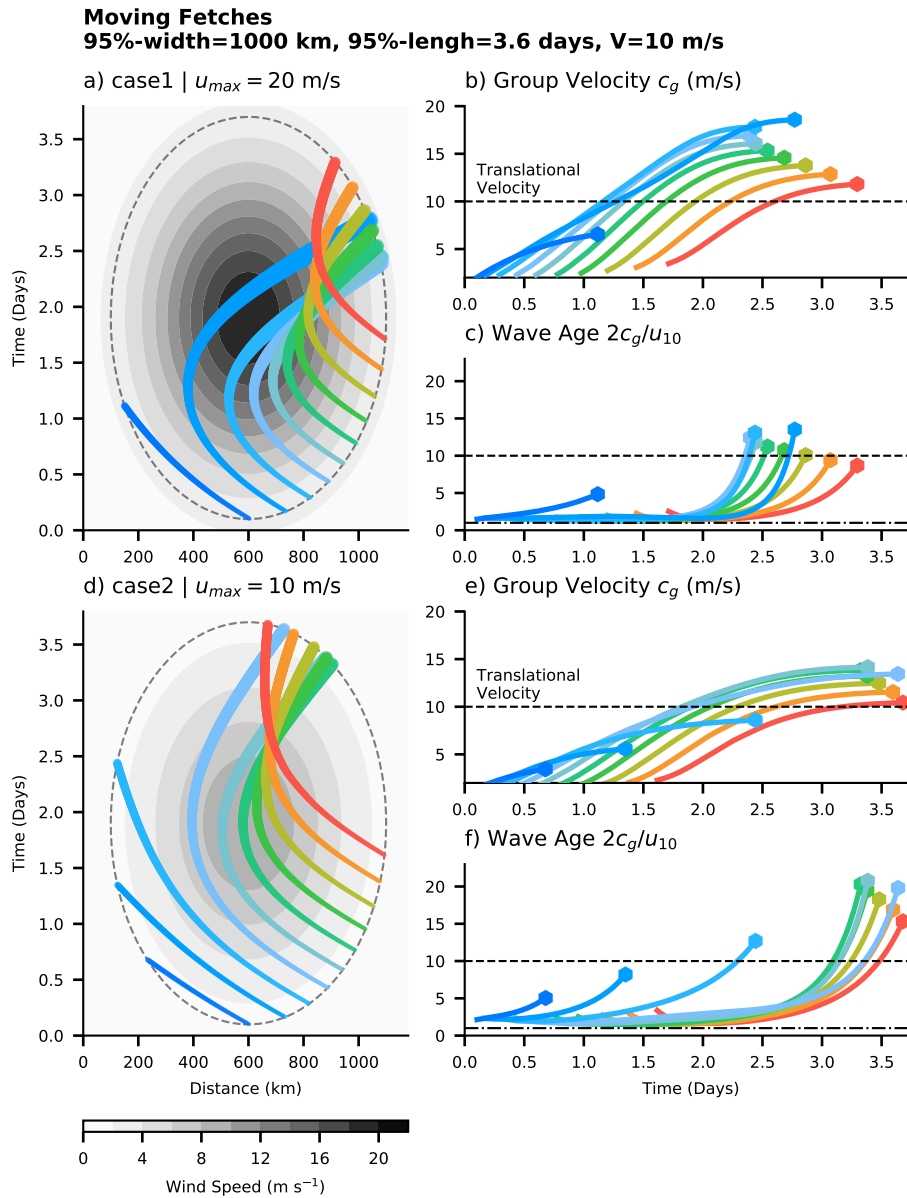


**Figure 5.** Characteristic curves from two-dimensional Gaussian winds in the moving frame of reference. a) two-dimensional Gaussian wind forcing (gray shading) with characteristic curves (colored lines) within the 95%-extension of the winds (black dashed lines). The wind forcing is defined by a 95%-width of 1000 km, a 95%-duration of 3.6 days, a translational velocity  $V$  of  $10 m s^{-1}$  and peak wind speed  $u_{max}$  of  $20 m s^{-1}$ . b) Group velocity along the characteristic curves as a function of time with colors same as in a). The translational velocity  $V = 10 m s^{-1}$  is shown as black dashed line. c) Same as in b) but for wave age  $\alpha = 2c_g/u_{10}$ . The dashed-dotted and dashed line indicate  $\alpha=1$  or  $10$  respectively. d) to f) as as a) to c) but for peak wind speed  $u_{max}=10 m s^{-1}$  rather than  $u_{max}=20 m s^{-1}$ .

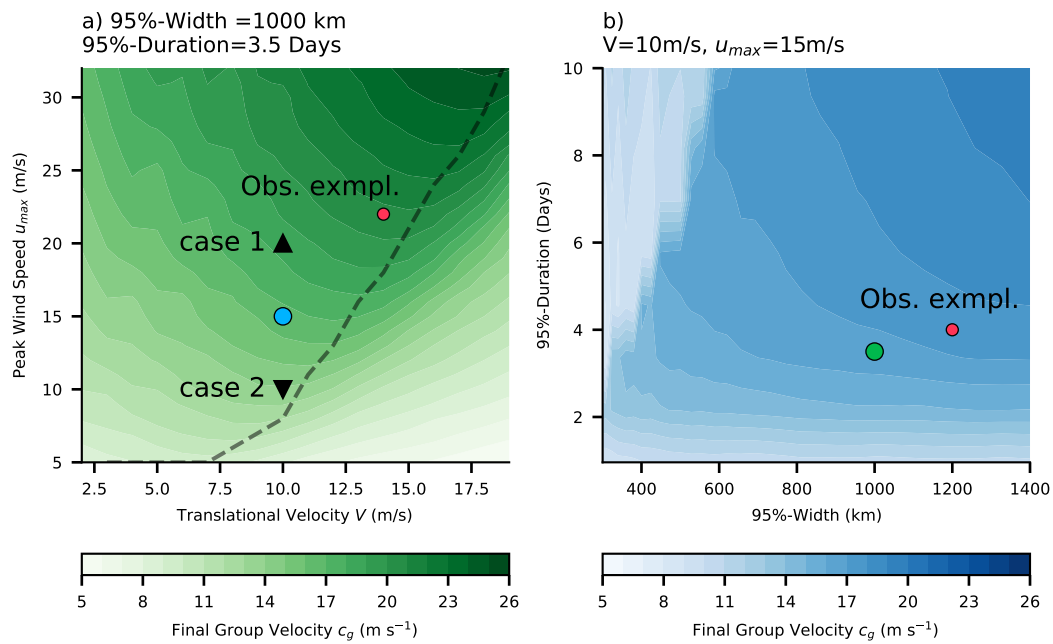


**Figure 6.** The dependences of the largest generated group velocity from the two-dimensional Gaussian wind model on the storm’s scales. a) Largest generated group velocities for varying translational velocity  $V$  and peak wind speed  $u_{max}$ . The dashed black line separates fetch- and time-limited cases. Case 1 and 2 from Figure 5 are shown as the black upward- and downward pointing triangles. b) Same as a) but for changes in the 95%-width and 95%-duration. The parameter space of a) and b) are represented as green or blue dot in the respective other panel. The observational case from section 3 (Figure 9c) is shown as red dot in a) and b).

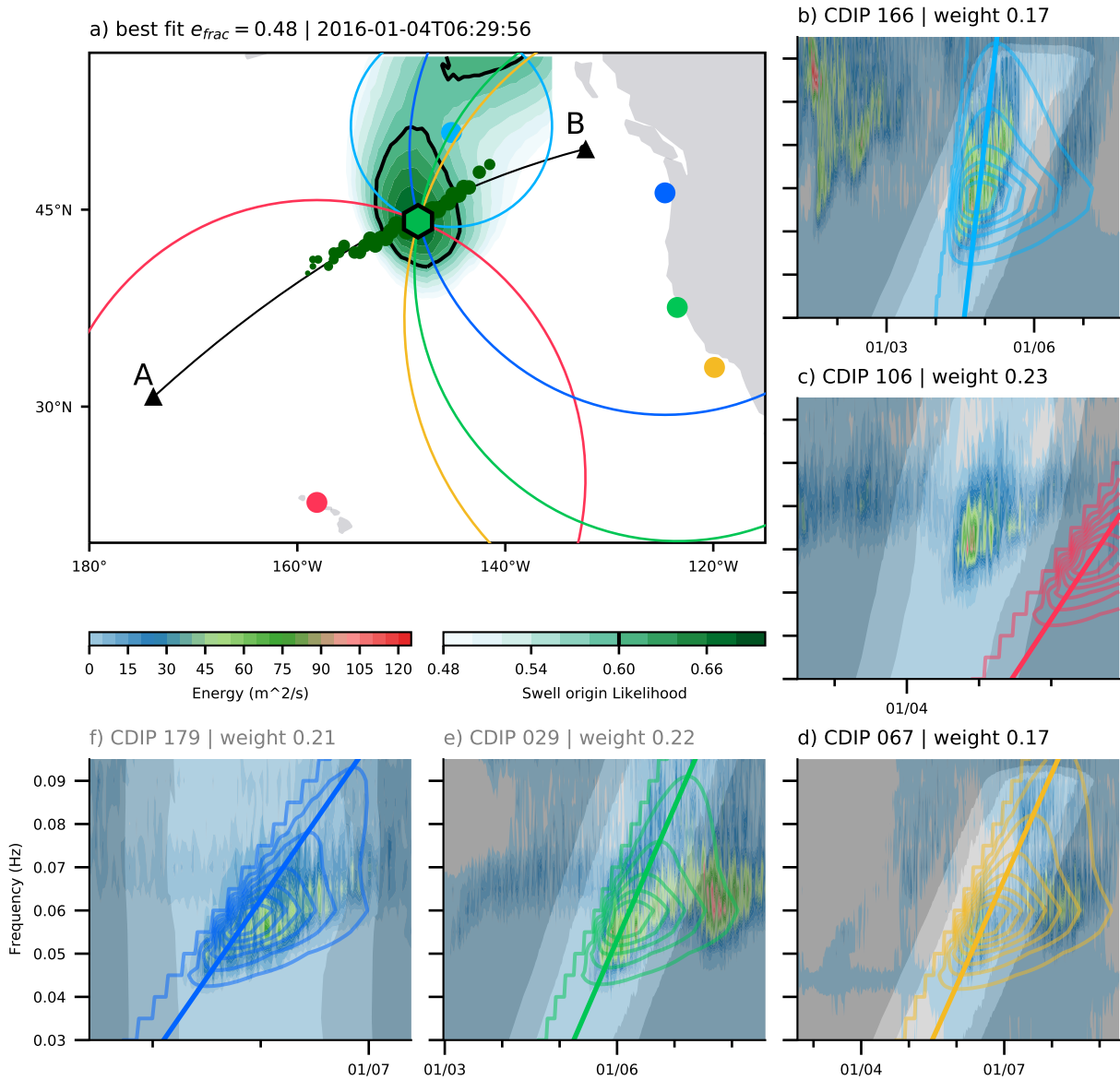


**Figure 7.** Results for the source point optimization for the case study in January 2016. a) The colored circles show the best fit great-circle distanced for the respective stations (colored dots). The great-circle radii correspond to the sloped lines in panel b to f and the green hexagon is the position of the most likely common origin on January 4th 2016 at 06:00 UTC. The green shading shows the the likelihood measure  $L_{ef} > 0.5$  for this time step and the black contour the corresponding likelihood of  $L_{ef} = 0.6$ . (b) to (f) The fitted parametric models (contours) compared to the station data (colored shading). The gray shadings in panel (b) to (f) is the weighting on the data during the optimization, and the weight in the sub-titles is the data's weight in the multi-station cost function (Suppl. Material T1).

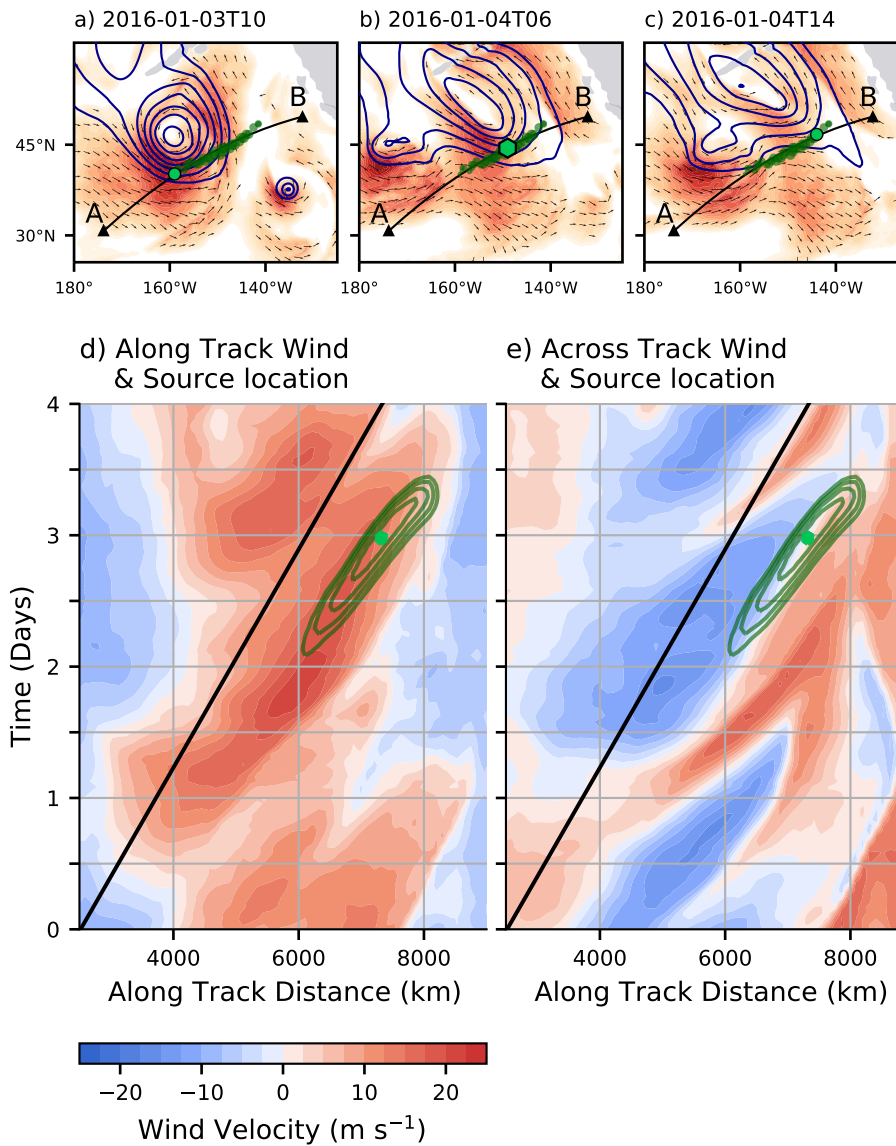


**Figure 8.** Optimized source locations compared to reanalysis winds (shading and vectors as in Figure 1) and negative SLP anomaly (dark blue contours as in Figure 1) for a date early in the event (a, 2016-01-03 10:00), the most likely origin time (b, 2016-01-04 04:00), and late in the event (c, 2016-01-04 14:00). The light green dots or the hexagon represent the most likely swell wave origin for the respective time step and the dark green dots are most likely swell wave origins for all time steps. The black line between the point A and B is a least-square fit to these dots of most likely origin and defines the transect through the wind data in panel d) and e). The transect through the wind data between point A and B is shown for along-transect (d) and across transect (e) winds. The wind data is indicated in red and blue shading, the area observed of most likely wave origin as green contours ( $L_{ef} \geq 0.6$ ), and its maximum as green hexagon. The estimated translational velocity along the transect is shown as black line (see suppl. Material F2).

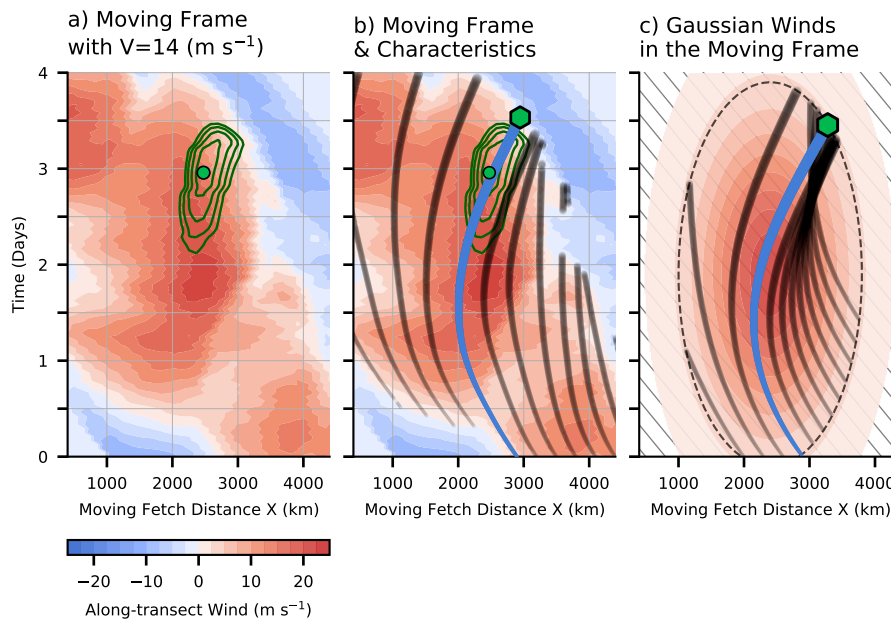


**Figure 9.** Observed winds in the moving frame of reference. a) Same as figure 8d but in the moving frame of reference. The black line figure 8d would be here a vertical line. b) Same as a) but with characteristic curves of  $\omega_p$  solving Equation 4 with the method of characteristics. c) Same as Figure 5a but for scale estimated from (b): 95%-width = 2800 km, 95%-duration = 4 days,  $u_{max} = 22 \text{ m s}^{-1}$ , and  $V = 14.1 \text{ m s}^{-1}$ . The characteristic curves with the highest wave energy are marked as blue line in panel b and c and the green hexagon indicates the position where wave growth can terminate the latest. The dashed black line in (c) is the 95%-boundary of the forcing field.

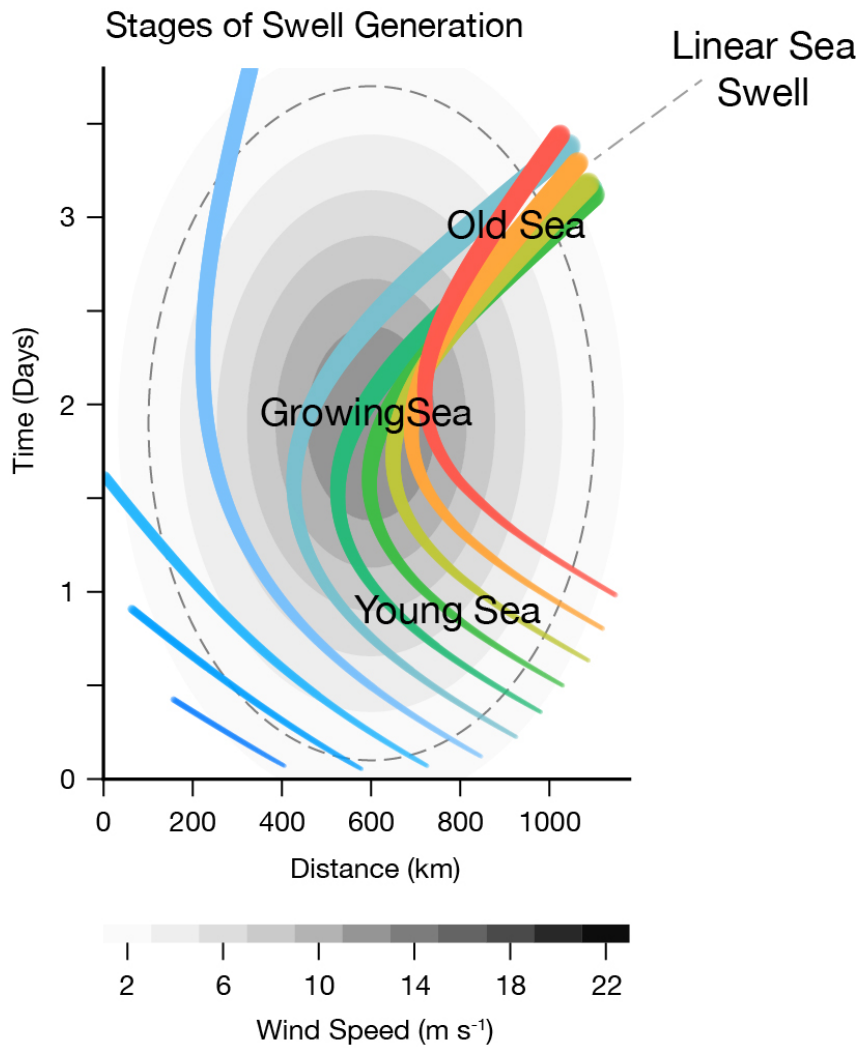


**Figure 10.** Schematic of wave growth under a moving storm with Gaussian wind. The gray shading shows the wind forcing and the dashed gray line marks the 95%-boundary of the Gaussian wind forcing. The colored lines are characteristic curves of wave generation in the reference system of moving extra-tropical storm. Wave growth starts with a *young sea* from rest and a small peak group speed. It develops into a *growing sea* that travels at the speed of the storm, until the wind forcing retires such that the sea state eventually stops growing and the non-linear wave-growth terms decay. Once the wave energy in each frequency band is dominantly linear the wave energy disperses and travel as *linear sea*, i.e. swell.

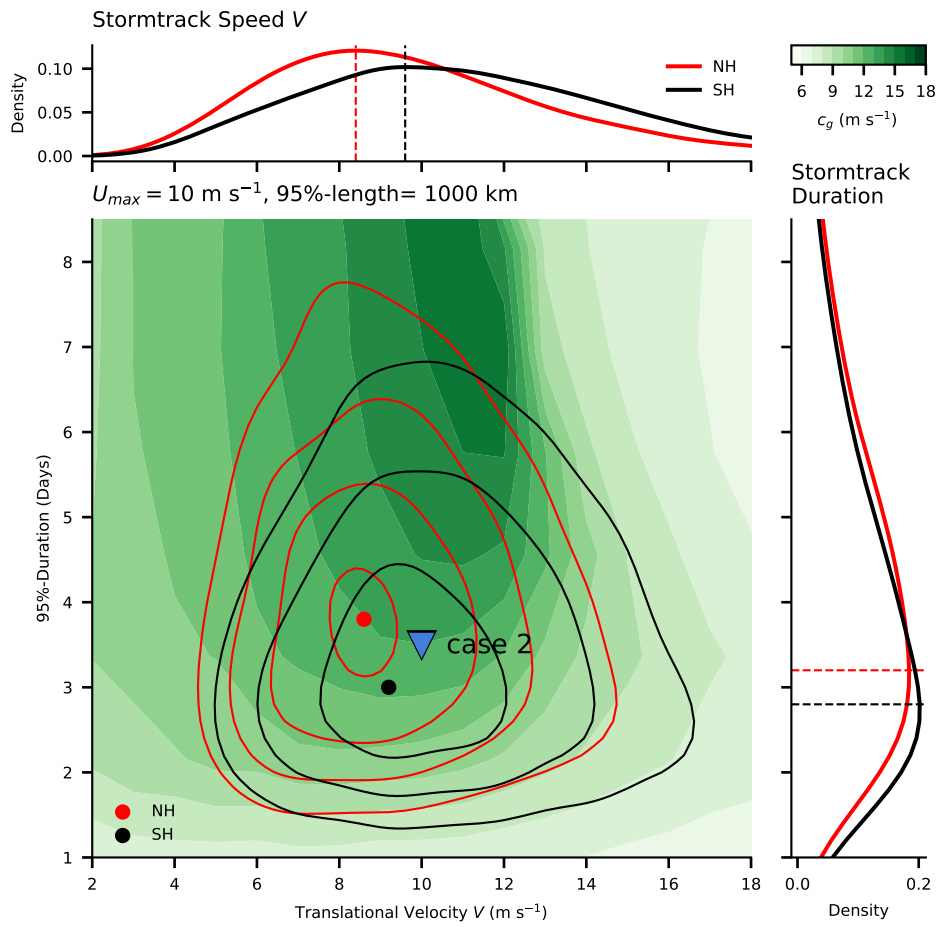


**Figure 11.** Peak group velocity  $c_g$  of wave events from a Gaussian wind forcing of different velocity  $V$  and duration. The given peak wind speed and 95%-width are predefined as  $u_{max} = 10 \text{ m s}^{-1}$  and 1000 km. The joint distributions of storm track speeds and lifetime are shown for the Northern Hemisphere (red) and Southern Hemisphere (black) as contours and their maxima as colored dots. The results for scales of a Gaussian wind forcing as in Figure 5d to f are shown as blue triangle. The storm track statistics are derived from reanalysis sea level pressure fields using Murray and Simmonds (1991a) and Murray and Simmonds (1991b). Note that this algorithm does not provide a peak wind speed  $u_{max}$  such that we assume  $10 \text{ m s}^{-1}$ , even though we point out that  $u_{max}$  is an important parameter for the resulting peak group velocity.

702 MH and AA thank Bruce Cornuelle and Sarah Gille for discussing topics related  
 703 to this paper. This is part of MH Phd thesis and was supported by the NASA grant 80NSSC19K0059.  
 704 AA was funded by a CNES post-doctoral grant. We thank Laure Baratgin for her help  
 705 during her summer internship at Scripps Institution of Oceanography and Leonidas Tsopouridis  
 706 for providing the storm track data.

707 **References**

708 Allen, S., Ferro, C. A. T., & Kwasniok, F. (2020). Recalibrating wind-speed fore-  
 709 casts using regime-dependent ensemble model output statistics. *Q. J. R. Mete-*  
 710 *orol. Soc.*, *146*, 2576–2596. doi: 10.1002/qj.3806

711 Andrews, D. G., & McIntyre, M. E. (1976, November). Planetary waves  
 712 in horizontal and vertical shear: The generalized Eliassen-Palm relation  
 713 and the mean zonal acceleration. *J. Atmos. Sci.*, *33*, 2031–2048. doi:  
 714 10.1175/1520-0469(1976)033<2031:PWIHAV>2.0.CO;2

715 Aouf, L., Hauser, D., Chapron, B., Toffoli, A., Tourain, C., & Peureux, C. (2021).  
 716 New Directional Wave Satellite Observations: Towards Improved Wave Fore-  
 717 casts and Climate Description in Southern Ocean. *Geophys. Res. Lett.*, *48*,  
 718 e2020GL091187. doi: 10.1029/2020GL091187

719 Ardhuin, F., Chapron, B., & Collard, F. (2009, March). Observation of  
 720 swell dissipation across oceans. *Geophys. Res. Lett.*, *36*, L06607. doi:  
 721 10.1029/2008GL037030

722 Ayet, A., Chapron, B., Redelsperger, J. L., Lapeyre, G., & Marié, L. (2020,  
 723 March). On the Impact of Long Wind-Waves on Near-Surface Turbu-  
 724 lence and Momentum Fluxes. *Bound.-Layer Meteorol.*, *174*, 465–491. doi:  
 725 10.1007/s10546-019-00492-x

726 Badulin, S. I., Babanin, A. V., Zakharov, V. E., & Resio, D. (2007, November).  
 727 Weakly turbulent laws of wind-wave growth. *J. Fluid Mech.*, *591*, 339–378.  
 728 doi: 10.1017/S0022112007008282

729 Barber, N. F., & Ursell, F. (1948, February). The generation and propagation of  
 730 ocean waves and swell. I. Wave periods and velocities. *Phil. Trans. R. Soc.*  
 731 *Lond. A*, *240*, 527–560. doi: 10.1098/rsta.1948.0005

732 Behrens, J., Thomas, J., Terrill, E., & Jensen, R. (2019, March). CDIP: Maintaining  
 733 a Robust and Reliable Ocean Observing Buoy Network. In *2019 IEEE/OES*

- 734 *Twelfth Current, Waves and Turbulence Measurement (CWTM)* (pp. 1–5). San  
 735 Diego, CA, USA: IEEE. doi: 10.1109/CWTM43797.2019.8955166
- 736 Bengtsson, L., Hodges, K. I., & Keenlyside, N. (2009, May). Will Extratropical  
 737 Storms Intensify in a Warmer Climate? *J. Climate*, *22*, 2276–2301. doi: 10  
 738 .1175/2008JCLI2678.1
- 739 Bengtsson, L., Hodges, K. I., & Roeckner, E. (2006, August). Storm Tracks and Cli-  
 740 mate Change. *J. Climate*, *19*, 3518–3543. doi: 10.1175/JCLI3815.1
- 741 Bjerknes, J. (1919, February). On the structure of moving cyclones. *Mon. Wea.*  
 742 *Rev.*, *47*, 95–99. doi: 10.1175/1520-0493(1919)47<95:OTSOMC>2.0.CO;2
- 743 Bourassa, M. A., Gille, S. T., Bitz, C., Carlson, D., Cerovecki, I., Clayson, C. A., ...  
 744 Wick, G. A. (2013, March). High-Latitude Ocean and Sea Ice Surface Fluxes:  
 745 Challenges for Climate Research. *Bull. Amer. Meteor. Soc.*, *94*, 403–423. doi:  
 746 10.1175/BAMS-D-11-00244.1
- 747 Bourassa, M. A., Meissner, T., Cerovecki, I., Chang, P. S., Dong, X., De Chiara,  
 748 G., ... Wentz, F. (2019). Remotely Sensed Winds and Wind Stresses  
 749 for Marine Forecasting and Ocean Modeling. *Front. Mar. Sci.*, *6*. doi:  
 750 10.3389/fmars.2019.00443
- 751 Bowyer, P. J., & MacAfee, A. W. (2005, June). The Theory of Trapped-Fetch  
 752 Waves with Tropical Cyclones—An Operational Perspective. *Weather Fore-*  
 753 *cast.*, *20*, 229–244. doi: 10.1175/WAF849.1
- 754 Cardone, V. J., Jensen, R. E., Resio, D. T., Swail, V. R., & Cox, A. T. (1996,  
 755 February). Evaluation of Contemporary Ocean Wave Models in Rare Ex-  
 756 treme Events: The “Halloween Storm” of October 1991 and the “Storm of  
 757 the Century” of March 1993. *J. Atmos. Oceanic Technol.*, *13*, 198–230. doi:  
 758 10.1175/1520-0426(1996)013<0198:EOCOWM>2.0.CO;2
- 759 Catto, J. L. (2018, June). A New Method to Objectively Classify Extratropical Cy-  
 760 clones for Climate Studies: Testing in the Southwest Pacific Region. *J. Clim.*,  
 761 *31*, 4683–4704. doi: 10.1175/JCLI-D-17-0746.1
- 762 Cavaleri, L. (1994). Applications to wave hindcasting and forecasting; Chapter  
 763 IV. In *Dynamics and Modeling of Ocean Waves* (p. 532). Cambridge Univer-  
 764 sity Press, USA.
- 765 Cavaleri, L. (2009, November). Wave Modeling-Missing the Peaks. *J. Phys.*  
 766 *Oceanogr.*, *39*, 2757–2778. doi: 10.1175/2009JPO4067.1

- 767 (CDS), C. C. C. S. C. D. S. (2017, June). *Copernicus Climate Change Service (C3S)*  
 768 *(2017): ERA5: Fifth generation of ECMWF atmospheric reanalyses of the*  
 769 *global climate.*
- 770 Chapron, B., Johnsen, H., & Garello, R. (2001, November). Wave and wind retrieval  
 771 from sar images of the ocean. *Ann. Télécommun.*, *56*, 682–699. doi: 10.1007/  
 772 BF02995562
- 773 Charney, J. (1947). The Dynamics of Long Waves in a Baroclinic Westerly Current.  
 774 *J. Meteorol.*, *4*, 135–162.
- 775 Chen, S. S., Price, J. F., Zhao, W., Donelan, M. A., & Walsh, E. J. (2007). The  
 776 CBLAST-Hurricane Program and the Next-Generation Fully Coupled Atmo-  
 777 sphere–Wave–Ocean Models for Hurricane Research and Prediction. *Bull. Am.*  
 778 *Meteorol. Soc.*, *88*, 311–317.
- 779 Collard, F., Ardhuin, F., & Chapron, B. (2009). Monitoring and analysis of ocean  
 780 swell fields from space: New methods for routine observations. *J. Geophys.*  
 781 *Res. Oceans*, *114*. doi: 10.1029/2008JC005215
- 782 Doyle, J. D. (1995, October). Coupled ocean wave/atmosphere mesoscale model sim-  
 783 ulations of cyclogenesis. *Tellus A*, *47*, 766–778. doi: 10.1034/j.1600-0870.1995  
 784 .00119.x
- 785 Doyle, J. D. (2002, December). Coupled Atmosphere–Ocean Wave Simulations un-  
 786 der High Wind Conditions. *Mon. Wea. Rev.*, *130*, 3087–3099. doi: 10.1175/  
 787 1520-0493(2002)130<3087:CAOWSU>2.0.CO;2
- 788 Durrant, T. H., Greenslade, D. J. M., & Simmonds, I. (2013, October). The effect  
 789 of statistical wind corrections on global wave forecasts. *Ocean Modelling*, *70*,  
 790 116–131. doi: 10.1016/j.ocemod.2012.10.006
- 791 Dysthe, K. B., & Harbitz, A. (1987). Big waves from polar lows? *Tellus A*, *39A*,  
 792 500–508. doi: 10.1111/j.1600-0870.1987.tb00324.x
- 793 Eady, E. T. (1949, January). Long Waves and Cyclone Waves. *Tellus*, *1*, 33–52. doi:  
 794 10.3402/tellusa.v1i3.8507
- 795 Edson, J. B., Jampana, V., Weller, R. A., Bigorre, S. P., Plueddemann, A. J.,  
 796 Fairall, C. W., ... Hersbach, H. (2013, May). On the Exchange of Mo-  
 797 mentum over the Open Ocean. *J. Phys. Oceanogr.*, *43*, 1589–1610. doi:  
 798 10.1175/JPO-D-12-0173.1
- 799 Elfouhaily, T., Chapron, B., Katsaros, K., & Vandemark, D. (1997, July). A unified

- 800 directional spectrum for long and short wind-driven waves. *J. Geophys. Res.*,  
 801 *102*, 15781–15796. doi: 10.1029/97JC00467
- 802 Enríquez, A. R., Marcos, M., Álvarez-Ellacuría, A., Orfila, A., & Gomis, D.  
 803 (2017, July). Changes in beach shoreline due to sea level rise and waves  
 804 under climate change scenarios: Application to the Balearic Islands (west-  
 805 ern Mediterranean). *Nat. Hazards Earth Syst. Sci.*, *17*, 1075–1089. doi:  
 806 10.5194/nhess-17-1075-2017
- 807 Fairall, C. W., Bradley, E. F., Hare, J. E., Grachev, A. A., & Edson, J. B. (2003,  
 808 February). Bulk Parameterization of Air–Sea Fluxes: Updates and Ver-  
 809 ification for the COARE Algorithm. *J. Climate*, *16*, 571–591. doi:  
 810 10.1175/1520-0442(2003)016<0571:BPOASF>2.0.CO;2
- 811 Feng, H., Vandemark, D., Quilfen, Y., Chapron, B., & Beckley, B. (2006, Au-  
 812 gust). Assessment of wind-forcing impact on a global wind-wave model  
 813 using the TOPEX altimeter. *Ocean Engineering*, *33*, 1431–1461. doi:  
 814 10.1016/j.oceaneng.2005.10.015
- 815 Ferreira, O. (SPR 2005). Storm groups versus extreme single storms: Predicted ero-  
 816 sion and management consequences. *J. Coast. Res.*, 221–227.
- 817 Gallet, B., & Young, W. R. (2014). Refraction of swell by surface currents. *J. Mar.*  
 818 *Res.*, *72*, 105–126. doi: info:doi/10.1357/002224014813758959
- 819 Gille, S. T. (2005, September). Statistical Characterization of Zonal and Meridional  
 820 Ocean Wind Stress. *J. Atmospheric Ocean. Technol.*, *22*, 1353–1372. doi: 10  
 821 .1175/JTECH1789.1
- 822 Hasselmann, K., Barnett, T. P., Bouws, E., Carlson, H., Cartwright, D. E., Enke,  
 823 K., ... Walden, H. (1973). Measurements of wind-wave growth and swell  
 824 decay during the Joint North Sea Wave Project (JONSWAP). *Ergänzungsheft*  
 825 *8-12*.
- 826 Hasselmann, K., Sell, W., Ross, D. B., & Müller, P. (1976, March). A Parametric  
 827 Wave Prediction Model. *J. Phys. Oceanogr.*, *6*, 200–228. doi: 10.1175/1520  
 828 -0485(1976)006<0200:APWPM>2.0.CO;2
- 829 Hasselmann, S., & Hasselmann, K. (1985, November). Computations and  
 830 Parameterizations of the Nonlinear Energy Transfer in a Gravity-Wave  
 831 Spectrum. Part I: A New Method for Efficient Computations of the Ex-  
 832 act Nonlinear Transfer Integral. *J. Phys. Oceanogr.*, *15*, 1369–1377. doi:

- 833 10.1175/1520-0485(1985)015<1369:CAPOTN>2.0.CO;2
- 834 Hauser, D., Tourain, C., Hermozo, L., Alraddawi, D., Aouf, L., Chapron, B., . . .  
 835 Tran, N. (2020). New Observations From the SWIM Radar On-Board  
 836 CFOSAT: Instrument Validation and Ocean Wave Measurement Assessment.  
 837 *IEEE Trans. Geosci. Remote Sens.*, 1–22. doi: 10.1109/TGRS.2020.2994372
- 838 Hell, M. C., Cornuelle, B. D., Gille, S. T., & Lutsko, N. J. (2021, April). Time-  
 839 Varying Empirical Probability Densities of Southern Ocean Surface Winds:  
 840 Linking the Leading Mode to SAM and Quantifying Wind Product Differences.  
 841 *J. Clim.*, -1, 1–80. doi: 10.1175/JCLI-D-20-0629.1
- 842 Hell, M. C., Cornuelle, B. D., Gille, S. T., Miller, A. J., & Bromirski, P. D. (2019,  
 843 October). Identifying Ocean Swell Generation Events from Ross Ice Shelf Seis-  
 844 mic Data. *J. Atmos. Oceanic Technol.*, 36, 2171–2189. doi: 10.1175/JTECH-D  
 845 -19-0093.1
- 846 Hell, M. C., Gille, S. T., Cornuelle, B. D., Miller, A. J., Bromirski, P. D., & Craw-  
 847 ford, A. D. (2020). Estimating Southern Ocean Storm Positions With  
 848 Seismic Observations. *J. Geophys. Res. Oceans*, 125, e2019JC015898. doi:  
 849 10.1029/2019JC015898
- 850 Hodges, K. I., Lee, R. W., & Bengtsson, L. (2011, April). A Comparison  
 851 of Extratropical Cyclones in Recent Reanalyses ERA-Interim, NASA  
 852 MERRA, NCEP CFSR, and JRA-25. *J. Climate*, 24, 4888–4906. doi:  
 853 10.1175/2011JCLI4097.1
- 854 Hoskins, B. J., McIntyre, M. E., & Robertson, A. W. (1985). On the use and signif-  
 855 icance of isentropic potential vorticity maps. *Q.J.R. Meteorol. Soc.*, 111, 877–  
 856 946. doi: 10.1002/qj.49711147002
- 857 Hunt, I. A. (1961). Design of Sea-Walls and Breakwaters. *Trans. Am. Soc. Civ.*  
 858 *Eng.*, 126, 542–570.
- 859 Husson, R., Ardhuin, F., Collard, F., Chapron, B., & Balanche, A. (2012, August).  
 860 Revealing forerunners on Envisat’s wave mode ASAR using the Global Seismic  
 861 Network. *Geophys. Res. Lett.*, 39. doi: 10.1029/2012GL052334
- 862 Janssen, P. (2004). *The Interaction of Ocean Waves and Wind*. Cambridge: Cam-  
 863 bridge University Press. doi: 10.1017/CBO9780511525018
- 864 Janssen, P. A., & Bidlot, J.-R. (2018). Progress in Operational Wave Forecasting.  
 865 *Procedia IUTAM*, 26, 14–29. doi: 10.1016/j.piutam.2018.03.003

- 866 Jiang, H., Stopa, J. E., Wang, H., Husson, R., Mouche, A., Chapron, B., & Chen,  
 867 G. (2016). Tracking the attenuation and nonbreaking dissipation of  
 868 swells using altimeters. *J. Geophys. Res. Oceans*, *121*, 1446–1458. doi:  
 869 10.1002/2015JC011536
- 870 Kitaigorodskii, S. A. (1962). Applications of the theory of similarity to the analysis  
 871 of wind-generated wave motion as a stochastic process. *Izv Geophys Ser Acad*  
 872 *Sci USSR*, *1*, 105–117.
- 873 Klotz, B. W., Neuenschwander, A., & Magruder, L. A. (2020). High-Resolution  
 874 Ocean Wave and Wind Characteristics Determined by the ICESat-2  
 875 Land Surface Algorithm. *Geophys. Res. Lett.*, *47*, e2019GL085907. doi:  
 876 10.1029/2019GL085907
- 877 Kudryavtsev, V., Golubkin, P., & Chapron, B. (2015). A simplified wave enhance-  
 878 ment criterion for moving extreme events. *J. Geophys. Res. Oceans*, *120*,  
 879 7538–7558. doi: 10.1002/2015JC011284
- 880 Kudryavtsev, V., Yurovskaya, M., & Chapron, B. (2021). 2D Parametric Model for  
 881 Surface Wave Development Under Varying Wind Field in Space and Time. *J.*  
 882 *Geophys. Res. Oceans*, *126*, e2020JC016915. doi: 10.1029/2020JC016915
- 883 Li, Q., Reichl, B. G., Fox-Kemper, B., Adcroft, A. J., Belcher, S. E., Danabasoglu,  
 884 G., ... Zheng, Z. (2019). Comparing Ocean Surface Boundary Vertical Mix-  
 885 ing Schemes Including Langmuir Turbulence. *J. Adv. Model. Earth Syst.*, *11*,  
 886 3545–3592. doi: 10.1029/2019MS001810
- 887 Li, Q., Webb, A., Fox-Kemper, B., Craig, A., Danabasoglu, G., Large, W. G.,  
 888 & Vertenstein, M. (2016, July). Langmuir mixing effects on global cli-  
 889 mate: WAVEWATCH III in CESM. *Ocean Model.*, *103*, 145–160. doi:  
 890 10.1016/j.ocemod.2015.07.020
- 891 Makin, V. K. (2008, December). On the Possible Impact of a Following-Swell on the  
 892 Atmospheric Boundary Layer. *Boundary-Layer Meteorol.*, *129*, 469–478. doi:  
 893 10.1007/s10546-008-9320-z
- 894 Mbengue, C., & Schneider, T. (2016, October). Storm-Track Shifts under  
 895 Climate Change: Toward a Mechanistic Understanding Using Baroclinic  
 896 Mean Available Potential Energy. *J. Atmos. Sci.*, *74*, 93–110. doi:  
 897 10.1175/JAS-D-15-0267.1
- 898 Morison, M. L., & Imberger, J. (1992, July). Water-Level Oscillations in Esperance

- 899 Harbour. *J. Waterw. Port Coast. Ocean Eng.*, *118*, 352–367. doi: 10.1061/  
 900 (ASCE)0733-950X(1992)118:4(352)
- 901 Morrow, R., Fu, L.-L., Ardhuin, F., Benkiran, M., Chapron, B., Cosme, E., . . .  
 902 Zaron, E. D. (2019). Global Observations of Fine-Scale Ocean Surface To-  
 903 pography With the Surface Water and Ocean Topography (SWOT) Mission.  
 904 *Front. Mar. Sci.*, *6*. doi: 10.3389/fmars.2019.00232
- 905 Munk, W. H. (1947, April). Tracking storms by forerunners of swell. *J. Meteor.*, *4*,  
 906 45–57. doi: 10.1175/1520-0469(1947)004<0045:TSBFOS>2.0.CO;2
- 907 Munk, W. H., & Snodgrass, F. E. (1957, January). Measurements of southern swell  
 908 at Guadalupe Island. *Deep Sea Research (1953)*, *4*, 272–286. doi: 10.1016/  
 909 0146-6313(56)90061-2
- 910 Murray, R. J., & Simmonds, I. (1991a). A numerical scheme for tracking cyclone  
 911 centres from digital data. Part I: Development and operation of the scheme.  
 912 *Aust Meteor Mag*, *39*, 155–166.
- 913 Murray, R. J., & Simmonds, I. (1991b). A numerical scheme for tracking cyclone  
 914 centres from digital data. Part II: Application to January and July general  
 915 circulation model simulations. *Aust Meteor Mag*, *39*, 167–180.
- 916 Neiman, P. J., & Shapiro, M. A. (1993, August). The Life Cycle of an Ex-  
 917 tratropical Marine Cyclone. Part I: Frontal-Cyclone Evolution and Ther-  
 918 modynamic Air-Sea Interaction. *Mon. Wea. Rev.*, *121*, 2153–2176. doi:  
 919 10.1175/1520-0493(1993)121<2153:TLCOAE>2.0.CO;2
- 920 Neiman, P. J., Shapiro, M. A., & Fedor, L. S. (1993, August). The Life Cycle of an  
 921 Extratropical Marine Cyclone. Part II: Mesoscale Structure and Diagnostics.  
 922 *Mon. Wea. Rev.*, *121*, 2177–2199. doi: 10.1175/1520-0493(1993)121<2177:  
 923 TLCOAE>2.0.CO;2
- 924 Neu, U., Akperov, M. G., Bellenbaum, N., Benestad, R., Blender, R., Caballero,  
 925 R., . . . Wernli, H. (2012, September). IMILAST: A Community Effort to  
 926 Intercompare Extratropical Cyclone Detection and Tracking Algorithms. *Bull.*  
 927 *Amer. Meteor. Soc.*, *94*, 529–547. doi: 10.1175/BAMS-D-11-00154.1
- 928 O'Reilly, W. C., Olfe, C. B., Thomas, J., Seymour, R. J., & Guza, R. T. (2016, Oc-  
 929 tober). The California coastal wave monitoring and prediction system. *Coastal*  
 930 *Engineering*, *116*, 118–132. doi: 10.1016/j.coastaleng.2016.06.005
- 931 Osinski, R. D., & Radtke, H. (2020, March). Ensemble hindcasting of wind and

- 932 wave conditions with WRF and WAVEWATCH III driven by ERA5. *Ocean*  
 933 *Sci.*, *16*, 355–371. doi: 10.5194/os-16-355-2020
- 934 Pierson, W. J., & Moskowitz, L. (1964, December). A proposed spectral form for  
 935 fully developed wind seas based on the similarity theory of S. A. Kitaigorod-  
 936 skii. *J. Geophys. Res.*, *69*, 5181–5190. doi: 10.1029/JZ069i024p05181
- 937 Ponce, S., & Ocampo-Torres, F. J. (1998). Sensitivity of a wave model to wind vari-  
 938 ability. *J. Geophys. Res. Oceans*, *103*, 3179–3201. doi: 10.1029/97JC02328
- 939 Quilfen, Y., & Chapron, B. (2019). Ocean Surface Wave-Current Signatures From  
 940 Satellite Altimeter Measurements. *Geophys. Res. Lett.*, *46*, 253–261. doi: 10  
 941 .1029/2018GL081029
- 942 Ribal, A., & Young, I. R. (2019, December). Calibration and Cross Validation of  
 943 Global Ocean Wind Speed Based on Scatterometer Observations. *J. Atmos.*  
 944 *Oceanic Technol.*, *37*, 279–297. doi: 10.1175/JTECH-D-19-0119.1
- 945 Russell, P. E. (1993, November). Mechanisms for beach erosion during storms. *Con-*  
 946 *tinental Shelf Research*, *13*, 1243–1265. doi: 10.1016/0278-4343(93)90051-X
- 947 Schemm, S., & Wernli, H. (2014). The linkage between the warm and the cold  
 948 conveyor belts in an idealized extratropical cyclone. *J. Atmospheric Sci.*, *71*,  
 949 1443–1459.
- 950 Schultz, D. M., Bosart, L. F., Colle, B. A., Davies, H. C., Dearden, C., Keyser, D.,  
 951 ... Winters, A. C. (2018, January). Extratropical Cyclones: A Century of  
 952 Research on Meteorology’s Centerpiece. *Meteorol. Monogr.*, *59*, 16.1-16.56.  
 953 doi: 10.1175/AMSMONOGRAPHS-D-18-0015.1
- 954 Schultz, D. M., Keyser, D., & Bosart, L. F. (1998, July). The Effect of Large-Scale  
 955 Flow on Low-Level Frontal Structure and Evolution in Midlatitude Cyclones.  
 956 *Mon. Wea. Rev.*, *126*, 1767–1791. doi: 10.1175/1520-0493(1998)126<1767:  
 957 TEOLSF>2.0.CO;2
- 958 Shapiro, M. A., & Keyser, D. (1990). Fronts, jet streams, and the tropopause. Ex-  
 959 tratropical Cyclones, The Erik Palmén Memorial Volume, CW Newton and E.  
 960 Holopainen, Eds. *Amer Meteor Soc*, 167.
- 961 Shaw, T. A., Baldwin, M., Barnes, E. A., Caballero, R., Garfinkel, C. I., Hwang,  
 962 Y.-T., ... Voigt, A. (2016, September). Storm track processes and the  
 963 opposing influences of climate change. *Nature Geosci.*, *9*, 656–664. doi:  
 964 10.1038/ngeo2783

- 965 Sinclair, V. A., Rantanen, M., Haapanala, P., Räisänen, J., & Järvinen, H. (2020,  
 966 January). The characteristics and structure of extra-tropical cyclones in a  
 967 warmer climate. *Weather Clim. Dynam.*, *1*, 1–25. doi: 10.5194/wcd-1-1-2020
- 968 Snodgrass, F. E., Groves, G. W., Hasselmann, K. F., Miller, G. R., Munk, W. H.,  
 969 & Powers, W. H. (1966, May). Propagation of Ocean Swell across the Pa-  
 970 cific. *Philos. Trans. R. Soc. Lond. Math. Phys. Eng. Sci.*, *259*, 431–497. doi:  
 971 10.1098/rsta.1966.0022
- 972 Stopa, J. E., & Cheung, K. F. (2014, March). Intercomparison of wind and  
 973 wave data from the ECMWF Reanalysis Interim and the NCEP Cli-  
 974 mate Forecast System Reanalysis. *Ocean Modelling*, *75*, 65–83. doi:  
 975 10.1016/j.ocemod.2013.12.006
- 976 Tolman, H. L. (2009). User manual and system documentation of WAVEWATCH III  
 977 TM version 3.14. *Tech. Note MMAB Contrib.*, *276*, 220.
- 978 Trindade, A., Portabella, M., Stoffelen, A., Lin, W., & Verhoef, A. (2020, February).  
 979 ERAstar: A High-Resolution Ocean Forcing Product. *IEEE Trans. Geosci. Re-  
 980 mote Sensing*, *58*, 1337–1347. doi: 10.1109/TGRS.2019.2946019
- 981 Villas Bôas, A. B., Gille, S. T., Mazloff, M. R., & Cornuelle, B. D. (2017, Novem-  
 982 ber). Characterization of the Deep Water Surface Wave Variability in the Cal-  
 983 ifornia Current Region. *J. Geophys. Res. Oceans*, *122*, 8753–8769. doi: 10  
 984 .1002/2017JC013280
- 985 Villas Bôas, A. B., & Young, W. R. (2020, May). Directional diffusion of surface  
 986 gravity wave action by ocean macroturbulence. *J. Fluid Mech.*, *890*. doi: 10  
 987 .1017/jfm.2020.116
- 988 Wentz, F. J., Scott, R., Hoffman, R., Leidner, S. M., Atlas, R., & Ardizzone,  
 989 J. (2015). *Remote Sensing Systems Cross-Calibrated Multi-Platform  
 990 (CCMP) 6-hourly ocean vector wind analysis product on 0.25 deg grid, Ver-  
 991 sion 2.0. Remote Sensing Systems, Santa Rosa, CA. Available online at  
 992 www.remss.com/measurements/ccmp.*
- 993 Wilson, B. (1957). Origin and effects of long period wave in ports. *Proc 19th Int  
 994 Navig Cong Sect II Commun I*, 13–61.
- 995 Young, I. R. (1988, September). Parametric Hurricane Wave Prediction Model.  
 996 *J. Waterw. Port Coast. Ocean Eng.*, *114*, 637–652. doi: 10.1061/(ASCE)0733  
 997 -950X(1988)114:5(637)

- 1098 Young, I. R. (2003, May). A review of the sea state generated by hurricanes. *Marine*  
 1099 *Structures*, *16*, 201–218. doi: 10.1016/S0951-8339(02)00054-0
- 1000 Young, I. R., Hasselmann, S., & Hasselmann, K. (1987, September). Computations  
 1001 of the Response of a Wave Spectrum to a Sudden Change in Wind Direction.  
 1002 *J. Phys. Oceanogr.*, *17*, 1317–1338. doi: 10.1175/1520-0485(1987)017<1317:  
 1003 COTROA>2.0.CO;2
- 1004 Young, I. R., & Vinoth, J. (2013, September). An “extended fetch” model for the  
 1005 spatial distribution of tropical cyclone wind–waves as observed by altimeter.  
 1006 *Ocean Engineering*, *70*, 14–24. doi: 10.1016/j.oceaneng.2013.05.015
- 1007 Zakharov, V. E., & Badulin, S. I. (2011, October). On energy balance in wind-driven  
 1008 seas. *Dokl. Earth Sc.*, *440*, 1440–1444. doi: 10.1134/S1028334X11100175
- 1009 Zakharov, V. E., Badulin, S. I., Geogjaev, V. V., & Pushkarev, A. N. (2019). Weak-  
 1010 Turbulent Theory of Wind-Driven Sea. *Earth Space Sci.*, *6*, 540–556. doi: 10  
 1011 .1029/2018EA000471
- 1012 Zou, Z., Li, S., Huang, J., Li, P., Song, J., Zhang, J. A., & Wan, Z. (2020, May).  
 1013 Atmospheric Boundary Layer Turbulence in the Presence of Swell: Tur-  
 1014 bulent Kinetic Energy Budget, Monin–Obukhov Similarity Theory, and  
 1015 Inertial Dissipation Method. *J. Phys. Oceanogr.*, *50*, 1213–1225. doi:  
 1016 10.1175/JPO-D-19-0136.1